A Proof-of-Concept Capillary-Fed Architecture for CO_2-to-CO Electrolysis

Master Thesis Report

by

Thoriq Fauzan Ariandi

Student Number
6290396

to obtain the degree of
Master of Science in Sustainable Energy Technology at Delft University of Technology,
to be defended publicly in Delft, July 21, 2026, at 10:00.

Project duration:	November 11, 2025 – July 14, 2026
Main Supervisor:	Dr. ir. David A. Vermaas
Daily Supervisor:	Sten de Roon
Thesis Committee:	Dr. ir. David A. Vermaas
	Dr. ir. Tom. E. Burdiny
	Dr. Bijoy Bera
Institutions:	Delft University of Technology
Faculty:	Faculty of Applied Science, TU Delft

TU Delft lpdp

Abstract

Carbon dioxide (CO_2) electrolysis is a promising technology for producing carbon-neutral chemical feedstocks. However, further improvements in energy efficiency and system cost are required before large-scale deployment can be realized. Capillary-fed electrolysis (CFE), originally developed for water electrolysis, has revealed lower cell overpotentials by providing relatively bubble-free environments in which gas products can readily leave the cell. This study investigates the implementation of CFE for CO_2-to-CO electrolysis and aims to identify the operating principles governing its effective application.

Our CFE cell, employing a porous polyethersulfone (PES) membrane and alkaline electrolyte, is successfully demonstrated. Comparison with an AEM-based hybrid-MEA cell confirms that the CFE cell operates at lower cell potential. However, an initial voltage increase not observed in conventional cell architecture is identified. The increase is attributed to CO_2 bubbles forming inside the membrane through (bi)carbonate neutralization, which increase the ohmic overpotential by blocking ion transport and the kinetic overpotential by locally increasing the current density through bubble coverage of the cathode active area.

During longer-term operation, water management and electrolyte concentration determine the product selectivity of the CFE cell. The use of a porous membrane in a CFE cell enables control over the water supply unavailable in other architectures, which can be realized through selection of membrane pore size, cell compression, and CO_2 feed humidification. A balance between cathode flooding and salt supersaturation is key to achieving optimal water supply. In addition, electrolyte concentration is found to contribute more strongly to salt precipitation than to promoting carbon-product formation. These findings establish key design principles for implementing capillary-fed CO_2 electrolysis. Despite the need for further research to enhance stability and product selectivity, the proposed CFE cell has shown potential cost reduction through its simplified system setup and the use of lower-cost membrane materials.

Contents

List of Figures

Abbreviations

Abbreviation	Description
AEM	Anion Exchange Membrane
CEM	Cation Exchange Membrane
CL	Catalyst Layer
CO2RR	CO_2 Reduction Reaction
FE	Faradaic Efficiency
GC	Gas Chromatography
GDE	Gas Diffusion Electrode
GDL	Gas Diffusion Layer
HER	Hydrogen Evolution Reaction
MEA	Membrane-Electrode Assembly
MPL	Microporous Layer
OER	Oxygen Evolution Reaction
PES	Polyether Sulfone

1

Introduction

Hard-to-abate sectors, such as the chemical, shipping, and aviation industries [1], cannot entirely rely on electrification to reduce their carbon emissions. The chemical industry requires not only electricity but also basic molecules as feedstocks. Meanwhile, due to the scale required for shipping and aviation, the energy density of current battery technologies precludes their use as solutions [2]. Since these sectors are currently fueled by fossil fuels, a viable decarbonization pathway is to synthesize the fuel from captured CO_2, thereby decarbonizing downstream industries.

CO_2 electrolysis emerges as a possible technological solution that can directly convert CO_2 from emissions back into value-added products, thus offering a pathway to close the carbon cycle. One of the possible and simplest products of CO_2 electrolysis is CO, which can be further processed to produce higher hydrocarbons via the Fischer-Tropsch (FT) process. However, CO_2 electrolysis technology is still in development with pilot or test plants rather than full-scale industrial facilities. For low-temperature CO_2 electrolysis, the technological readiness level (TRL) is currently at 5 to 6 [3].

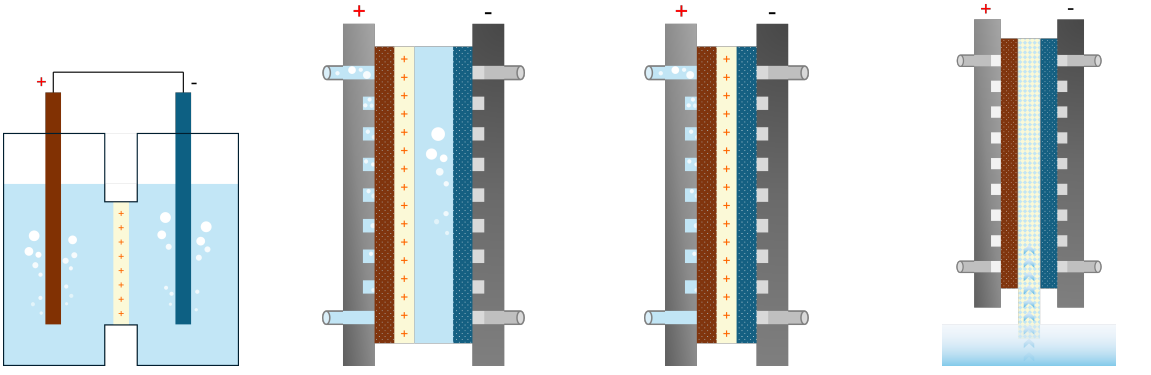

(a) H-cell configuration. **(b)** Flow-cell configuration. **(c)** Zero-gap Hybrid-MEA configuration. **(d)** CFE cell configuration.

Figure 1.1: A schematic overview of the development of CO_2 electrolysis cells.

Figure 1.1 illustrates the development of the cell architecture since its advent. Significant performance improvement over its initial introduction, which was performed in a 2-compartment cell, also called an H-cell (Fig 1.1a) [4], has been achieved through the adoption of gas-diffusion electrodes (GDEs). The use of GDEs solved the issue of low CO_2 solubility, which limits reactant mass transport, and made it possible to run the cell at industrially relevant current density [5]. With a GDE, the cell architecture evolves into a flow-cell configuration (Fig 1.1b), in which a catholyte liquid separates the cathode and the ion-exchange membrane

to provide hydration and pH regulation.

Next, further efficiency can be gained by removing the need for the catholyte flow, which adds an extra distance of ion conduction. This configuration, called the membrane-electrode assembly (MEA, Fig 1.1c), has the anode and cathode separated only by an ion-exchange membrane and is the latest iteration in cell design of CO_2 electrolyzers [6].

Even with the achieved optimization of MEA cells, further research is needed, as the efficiency of this configuration at higher current densities remains too low for commercial relevance [7]. Low CO_2 utilization and high cell potentials are also among the main challenges [8, 9]. Furthermore, improving the economics also requires reductions in the capital cost of the electrolyzer [10].

The recent idea of capillary-fed electrolysis (CFE), first proposed by [11] for water electrolysis, could further reduce the high cell potential and capital cost (Fig 1.1d). This configuration saw lower overpotential by eliminating the anolyte flow submerging the anode. Instead, the electrolyte is supplied via capillary action by a porous membrane placed between the electrodes. Without submerging the anode in anolyte, the formation of anodic gas bubbles that momentarily obscure the active cell area can be avoided. Another advantage is the simpler balance-of-plant required due to the elimination of the need for pumps to recirculate the electrolyte. This configuration thus reduces overall energy consumption and, therefore, potentially electrolyzer capital costs.

The CFE concept for water electrolysis has been further studied. Using a voltage fluctuation and acoustic detection technique, Hoang et al [12] found that the CFE setup does indeed produce substantially lower bubble formation rate compared to the conventional setup. The anode is essentially bubble-free up to $0.3\ A/cm^2$, with a rising formation rate with increasing current density. Tripathi et al. later found that the performance of CFE for water electrolysis correlates with temperature, applied torque, and separator thickness [13]. Higher temperature lowers the cell potential and increases ionic mobility; higher applied torque reduces interfacial contact resistance, and an increase in separator thickness enhances electrolyte availability, though it also increases the resistance.

Porous membrane (PM) is one of the distinguishing features of a CFE configuration. The use of PM has also been explored in the conventional setup as it provides several advantages. It features good mechanical properties, with many types commercially available and considerably cheaper than ion-exchange membranes [14]. Due to its non-selective property, PM can facilitate bidirectional ion transfer and thus is better at facilitating ionic balance under concentration polarization. It also exhibits significantly faster diffusion rates compared to Nafion-based membranes [15] and thereby lowers the electrolyte ohmic overpotential. A scaled-up 100 cm^2 cell utilizing a zero-gap anolyte flow electrolyzer with PM has achieved 100 hours of stable run at 200 mA/cm^2 with 80% CO selectivity [16]. This performance and economic reasons place porous membranes as a strong alternative to ion-exchange membrane dominance.

Inspired by the results of CFE configuration, this research project aims to apply that approach to the field of CO_2 electrolysis to determine whether similar performance gains can be achieved. For that matter, the main research question of this thesis project is to elucidate **what principles enable effective implementation of CFE in CO_2-to-CO electrolysis**.

Our experimental results show that CFE can indeed work for CO_2-to-CO electrolysis with comparable performance to that of a hybrid-MEA cell architecture using identical conditions. However, we observe an initial voltage peak not found to be reported in other work. As such phenomenon could affect the long-term performance of the studied CFE cell, we define our sub-research questions as follows:

1. What is the mechanism behind the initial voltage peak observed in CFE CO_2 electrolysis?
2. How do operating parameters affect the performance of a CFE CO_2 electrolysis cell in terms of voltage and selectivity?
3. How does a CFE cell compare to a hybrid-MEA CO_2 electrolysis cell?

This thesis report is structured as follows: chapter 2 discusses the relevant theoretical background of CO_2 electrolysis and the parasitic phenomena that hinder its stable operation. Additionally, the capillary action of a porous membrane unique to CFE architecture will also be discussed. Next, chapter 3 explains the material and experimental setup used to obtain the data. Chapter 4 then presents and discusses our findings in regard to the proposed research questions. Beginning with the CO_2 bubble blockage as the potential mechanism of the observed initial voltage peak, followed by the effect of electrolyte concentration and water management on the cell's performance stability, and finalized with a performance comparison to a hybrid-MEA cell. Finally, chapter 5 summarizes our findings that address our research questions, followed by several recommendations for experimental pathways in chapter 6 to elucidate further the mechanism governing the operation of a CFE cell.

2

Theoretical Background

In this chapter, the theoretical background relevant to the study of the CFE CO_2 electrolysis cell is covered. The discussion follows from the anodic and cathodic reactions involved in a CO_2 electrolysis cell, the competing hydrogen evolution reaction, and the parasitic (bi)carbonate buffer reaction. Furthermore, as we observe cathode flooding occurring in our cell, the cause of flooding and the subsequent salt precipitation are also explained. The section closes with a derivation of the equation that governs the capillary flow of a porous membrane, which is unique to a CFE cell.

2.1. CO_2-to-CO Electrolysis

CO_2 reduction reaction (CO_2RR) is a multi-proton and multi-electron transfer process carried out in an electrolyzer cell involving cathodic and anodic half-reactions. At the cathode, CO_2 undergoes a reduction reaction on the surface of a metal catalyst to form the product. Different metals have been found to promote greater selectivity for a specific product. For CO, silver (Ag) is more commonly used due to its lower cost [17]. At the anode, water or hydroxide anions are oxidized to form oxygen gas (O_2) in the oxygen evolution reaction (OER). Both of these reactions can proceed via either an acidic or alkaline pathway. In the alkaline pathway, half reactions in the cathode and anode are as follows:

$$\text{Cathode:} \quad CO_2 + H_2O + 2\,e^- \longrightarrow CO + 2\,OH^- \tag{2.1}$$

$$\text{Anode:} \quad 4\,OH^- \longrightarrow O_2 + 2\,H_2O + 4\,e^- \tag{2.2}$$

While in the acidic pathway, the half reactions are as follows:

$$\text{Cathode:} \quad CO_2 + 2\,H^+ + 2\,e^- \longrightarrow CO + H_2O \tag{2.3}$$

$$\text{Anode:} \quad 2\,H_2O \longrightarrow O_2 + 4\,H^+ + 4\,e^- \tag{2.4}$$

Although CO_2RR has been shown to work in acidic or alkaline electrolytes, an experiment by Yao et al [18] suggests that CO_2RR will tend to occur in a neutral or alkaline microenvironment. The experiment shows that H_2O, rather than H^+, serves as the proton source for the reaction, indicating a preference for the alkaline pathway. This view is supported in the investigation by Wu et al [19], who found that the reaction rate follows a first-order dependence on H^+ concentration at a low overpotential, which turns to zero-order at a higher overpotential. This finding indicates that the acidic pathway, in which H^+ is the proton donor, occurs only at the onset of the reaction, and that increasing the overpotential switches the proton donor to water. The alkaline pathway effectively becomes the preferred pathway for CO_2RR even when H^+ is abundant in the acidic bulk electrolyte.

At the cathode, abundance of water or proton can promote the competing hydrogen evolution reaction (HER), which is also an electrochemical reaction and thus consumes the electron

supply. HER can also proceed in the following two pathways:

$$\text{Alkaline:} \quad 2\,H_2O + 2\,e^- \longrightarrow H_2 + 2\,OH^- \tag{2.5}$$

$$\text{Acidic:} \quad 2\,H^+ + 2\,e^- \longrightarrow H_2 \tag{2.6}$$

This competition is quantified by selectivity or Faradaic efficiency (FE), which measures the fraction of the total supplied electric charge that participates in the reaction to form the target product, in this case, CO_2RR. If the reaction conditions increasingly favor HER, the system's efficiency is reduced because electrical power is spent on producing an undesired product.

In addition to pH effects, factors such as the presence of alkali cations can influence reaction selectivity, with larger cations reported to promote better performance. Under applied voltage, cations will adsorb to the cathode surface to help balance the charges. Larger cations have smaller hydration shells, which enable them to approach the electrode surface more closely. This closer encounter creates a stronger electric field, which strengthens the adsorption of CO_2RR reaction intermediates [20, 21]. Cations also act as buffering agents that lower the pH in the cathode microenvironment. The lower pH shifts the DIC concentration towards the CO_2(aq) form, which promotes CO_2RR. Larger cations have smaller pKa and thus larger buffering capacity in the order of $Cs^+ > Rb^+ > K^+ > Na^+ > Li^+$ [22]. The adsorption of partially desolvated cation on the catalyst surface could also block H^+ mobility to the surface, thus hindering HER. CO_2RR has even been reported to not proceed in the absence of alkali cation in the electrolyte [23, 24, 25]. Despite the important role, increasing the supply of the cation does not necessarily translate to higher selectivity toward carbon products [26], and higher concentration could even lead to increased salt precipitation detrimental for CO_2RR [27, 28]. In this regard, the larger Cs^+ cation has the benefit of higher salt solubility in water, lowering salt precipitation [16, 29].

In a practical cell, efficient delivery of the reactants to the reaction site is essential to performance. With a conventional H-cell, CO_2 gas has to diffuse through the bulk electrolyte in the form of CO_2(aq) to reach the reaction site at the cathode surface. This slow diffusion process greatly impedes the achievable reaction rate, measured in partial current density. Since CO_2 has low solubility, the reaction quickly hits the mass-transport limit. In a zero-gap cell, this limit is surpassed by adopting a gas diffusion electrode (GDE), which has a gas diffusion layer (GDL) through which gas can diffuse and a catalyst layer where catalytic reactions occur. The CO_2(g) then diffuses through the thin electrolyte layer covering the catalyst surface and participates in the reaction as CO_2(aq) [30]. The speed gain comes from the fact that now the CO_2 only has to travel in a nanometer-thick electrolyte coating on the catalyst surface as opposed to the up to centimeter-thick bulk electrolyte in the conventional H-cell setup.

After the reaction completes, the formed CO gas then exits via the GDL back to the cathode outlet. At the same time, the dissolved OH^- co-product is transported to the anode side, driven by drift from the applied electric field and diffusion due to the concentration gradient. The OH^- then becomes the reactant for alkaline OER.

As shown in equations (2.2) and (2.4), the oxygen evolution reaction can proceed via two pathways depending on the local pH at the reaction site. However, a simulation result by Fornaciari et al. [31] shows that a different initial bulk pH can yield a different equilibrium local pH. At very high (pH = 13) and very low (pH = 0) bulk electrolyte pH, the local pH at the reaction site stays at bulk pH during OER. Meanwhile, at near-neutral bulk electrolyte (pH = 9), performing OER at a current density of 30 mA/cm^2 drives the local pH to almost 2. This local acidification with a near-neutral-pH electrolyte indicates that OH^- is being depleted and that mass transport cannot keep up with the reaction rate. Furthermore, another simulation by Veroneau et al [32] shows that the drop in pH does not only occur when using near-neutral initial bulk pH: at a much higher current density of 1 A/cm^2, the local pH converges to pH 1 regardless of the bulk. This finding means that at high enough current density, the prevailing OER pathway will be acidic. Switching to an acidic OER pathway increases the voltage needed to keep the reaction, since the kinetics for oxidizing H_2O are harder compared to oxidizing OH^- [33].

2.2. Cell Potential

2.2.1. The Standard Cell Potential

The concept of standard cell potential is based on the thermodynamic understanding of a chemical reaction [34]. A chemical reaction performs work on its surroundings equal to the change in Gibbs energy per mol ΔG $[J/mol]$. The work is equal to the cell potential $[J/coulomb$ or V], which represents the work required to move a charge to the other electrode, multiplied by the amount of charge, which is equal to nF where n is the number of electrons and F is Faraday's constant. That gives the following relation:

$$\Delta G = -nFE \tag{2.7}$$

The negative sign indicates that, for a spontaneous reaction, the change in Gibbs energy is negative while the work done on the surroundings is positive. Thus E is positive for a spontaneous reaction requiring no energy input, and E^{θ} is then defined as the potential at standard conditions of 25 °C. Considering that each electrode hosts a half reaction, the full cell standard potential becomes the following:

$$E^{o}_{cell} = E^{o}_{cathode} - E^{o}_{anode} \tag{2.8}$$

The standard potential is defined in reference to the standard hydrogen electrode (SHE), set arbitrarily at 0 V. At pH 0, the cathodic CO_2RR standard potential (E^{θ}) is -0.52 V while the anodic OER is at 1.23 V vs SHE [17, 35], making the full cell potential of CO_2RR to -1.23 V. At different pH, the standard potential of each half reaction changes in relation to SHE. Nevertheless, the full-cell standard potential remains the same.

The standard potential, however, does change with temperature since the value is related to the change in Gibbs energy at standard 25 °C. For a CO_2RR with a full-cell reaction of $2\,CO_2 \longrightarrow 2\,CO + O_2$ and available thermodynamic data, a temperature increase will shift the potential in the positive direction, which means that increasing the reaction temperature will lead to a lower applied voltage required.

2.2.2. Overpotential

However, applying only the standard full cell potential to an electrolyzer will not drive the reaction. The required applied potential will comprise the thermodynamic, kinetic, and ohmic overpotentials [27]. The thermodynamic overpotential is the standard potential difference between the anodic and cathodic reactions, accounting for the dependence on species activities.

The thermodynamic potential is determined from the following expanded Nernst equation [34]:

$$E = E^{o}_{cell} - \frac{RT}{nF} \ln\left(\prod_{\substack{\text{ionic}\\ \text{species}}} \left(\frac{c_i}{c_i^{o}}\right)^{s_i} \prod_{\substack{\text{gas}\\ \text{species}}} \left(\frac{p_i}{p^{o}}\right)^{s_i} \right) \tag{2.9}$$

where E is the thermodynamic potential, E^{θ}_{cell} is the standard cell potential, and the $\prod_{\substack{\text{ionic}\\ \text{species}}} \left(\frac{c_i}{c_i^{o}}\right)^{s_i}$ and $\prod_{\substack{\text{gas}\\ \text{species}}} \left(\frac{p_i}{p^{o}}\right)^{s_i}$ terms each describes the reaction quotient of the dissolved ionic species and the gaseous species.

If we consider the activity of the gaseous species to be at normal conditions, the thermodynamic potential simplifies to the following [27]:

$$E_{\text{th}} = E^{o}_{cell} - \frac{RT}{F} \ln\left(\frac{c^{C}_{\text{OH}^-}}{c^{A}_{\text{OH}^-}}\right) \tag{2.10}$$

where $c^{C}_{\text{OH}^-}$ is the concentration of OH^- in the cathode and $c^{A}_{\text{OH}^-}$ is the concentration of OH^- in the anode. The term $\frac{RT}{F} \ln\left(\frac{c^{C}_{\text{OH}^-}}{c^{A}_{\text{OH}^-}}\right)$ then gives the thermodynamic or Nernstian overpotential

with high OH^- concentration in the cathode increases the thermodynamic potential (making it more negative) while high OH^- concentration in the anode lowers it (making it less negative). Considering the tendency for the CO_2RR system to have a local OH^- accumulation at the cathode and a local acidification at the anode as described in section 2.1, we can expect a significant Nernstian overpotential to arise.

Kinetic overpotential refers to the additional voltage required to drive reaction rates at the electrode surface. This additional voltage is due to the sluggish kinetics of CO_2RR, which involves several intermediate steps, each with its own activation energy, requiring an even more negative applied potential [17]. Kinetic overpotential is related to the Faradaic current by the Butler-Volmer equation described below [36]:

$$i = i_0 \left[e^{-\alpha f \eta} - e^{(1-\alpha) f \eta} \right] \tag{2.11}$$

with i_0 the exchange current, α the transfer coefficient, which ranges from zero to unity, η the kinetic overpotential, and $f = F/RT$. Meanwhile, the ohmic overpotential is the voltage drop due to the finite conductivity of ionic and electronic transport. Elevated temperature improves both the kinetics and the conductivity of ions.

2.3. Carbonate-Bicarbonate Reactions

CO_2RR in an alkaline electrolyte has the advantage of HER suppression compared to in acid environment. Nevertheless, alkaline CO_2RR suffers from parasitic (bi)carbonate formation by the reaction of OH^- and CO_2 as follows [9]:

$$CO_2 + OH^- \rightleftharpoons HCO_3^- \tag{2.12}$$

$$HCO_3^- + OH^- \rightleftharpoons CO_3^{2-} + H_2O \tag{2.13}$$

These reactions lower the utilization of CO_2 in alkaline electrolysis, that is, the ratio of CO_2 converted to the desired product over total converted CO_2. Reaction with OH^- caps the utilization efficiency to a maximum of 50% [37, 27]. This value follows from the fact that for every 1 mole of CO_2 converted to CO, there will be 2 moles of OH^- generated, which will then react with another 1 mole of CO_2 to make carbonate in the above cascading reaction. The utilization efficiency is even lower, at only 33% if the reaction stops at bicarbonate, which means that for every CO generated, two CO_2 are lost to become dissolved bicarbonate. Despite the parasitic nature, (bi)carbonate formation can lower the Nernstian overpotential in very alkaline bulk electrolyte by neutralizing the OH^- near the cathode surface and pushing the local pH down to near neutral [38].

In a more acidic environment, the formed (bi)carbonate can regenerate back to CO_2 by following the reaction:

$$CO_3^{2-} + H^+ \rightleftharpoons HCO_3^- \tag{2.14}$$

$$HCO_3^- + H^+ \rightleftharpoons CO_2 + H_2O \tag{2.15}$$

In zero-gap alkaline electrolyte CO_2RR, a similar neutralization occurs at the anode side. The (bi)carbonate will be transported to the anode side driven by drift and diffusion, where it will react with the H^+ generated by the anodic OER. This reaction converts the (bi)carbonate back into CO_2, which then degasses and escapes via the anode gas outlet, wasting the feed CO_2.

The above reactions are a set of reversible equilibrium reactions involving dissolved carbon dioxide, bicarbonate, and carbonate, collectively called dissolved inorganic carbon (DIC). The dominant species is dependent on the pH of the solution, as depicted in Figure 2.1. A buffer system is formed, since the species are acid-base conjugate pairs, with two pKa values. The intersections represent the pKa with $pK_{a1} = 6.35$ and $pK_{a2} = 10.33$.

Aside from wasting the CO_2 supply, the produced (bi)carbonate, coupled with alkali cations, can precipitate as salt crystals when their concentration reaches the solubility limit. The precipitate can block gas transport in the GDE, limiting the supply of CO_2 to the reaction site and thereby increasing HER. Salt blocking is strongly linked to cathode flooding, which enables the transport of salt to the cathode gas diffusion layer in the first place.

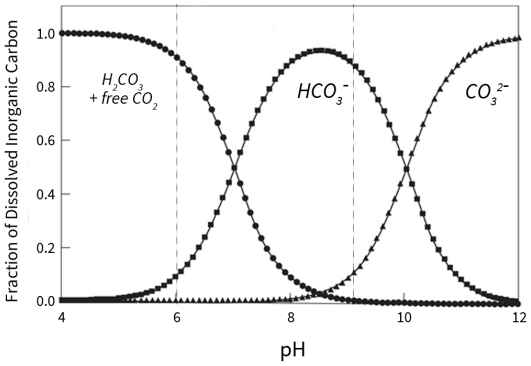

Figure 2.1: Speciation of dissolved inorganic carbon as a function of pH [39]

2.4. Cathode Flooding

A carbon-based GDE is typically constructed of a gas diffusion layer (GDL) and a catalyst layer (CL) [40]. The GDL further consists of the carbon fiber substrate (CFS) and the microporous layer (MPL). The CFS is the first porous layer through which CO_2 flows, positioned facing the cathode flow channel, and has added polytetraflouroethylene (PTFE) to increase its hydrophobicity. MPL is a composite made of carbon and PTFE with smaller, hydrophobic pores. This property means that penetrating liquid through the MPL requires higher liquid overpressure. The MPL also supports the catalyst deposited on top of it, forming the catalyst layer. The whole construct of GDL is designed to allow CO_2 diffusion into the catalyst layer, where it undergoes the catalytic reaction.

Flooding can be defined as the infiltration of electrolytes into the pore network of the GDE, reducing the GDE's effectiveness in transporting gas. With gas transport inhibited, the CO_2 concentration at the reaction site will be lower, and the dominant reaction shifts towards HER, as water will still be supplied sufficiently. The small and hydrophobic properties of the MPL pores help prevent water intrusion, as they increase the capillary pressure P_C or the pressure required for liquid to flow through, as described by the Young-Laplace equation:

$$P_C = \frac{2\gamma_{LG}\cos\theta}{r} \tag{2.16}$$

where γ_{LG} is the surface tension between the liquid and gas phase, θ is the contact angle characterizing hydrophobicity, and r the radius of the assumed cylindrical-shaped pore. Baumgartner et al [40] found that a GDL with a larger pore size distribution exhibits lower resistance to flooding since the largest pore size determines the minimum pressure at which the liquid starts to break through. If cracks are present, the MPL could be bypassed, allowing liquid to imbibe into the substrate layer and flood the GDL.

Flooding can occur if the surface loses its hydrophobicity, thereby reducing its capillary pressure. One such phenomenon is electrowetting, described as the reduction of the contact angle θ at a solid-electrolyte interface under an applied voltage [41]. By applying a voltage, the liquid electrolyte and solid surface hold opposing charges that attract each other, effectively lowering the free energy between the liquid and the solid and decreasing the solid-liquid surface tension γ_{SL} [42]. By Young's equation, decrease in γ_{SL} decreases the macroscopic contact angle θ:

$$\cos\theta = \frac{\gamma_{SG} - \gamma_{SL}}{\gamma_{LG}} \tag{2.17}$$

where the solid-gas surface tension (γ_{SG}) and liquid-gas surface tension (γ_{LG}) stay constant.

Baumgartner et al. [8], performed another investigation and found that flooding due to electrowetting is more severe in reactions requiring more negative cathode potential, indicating that electrolyte intrusion is indeed potential-dependent.

2.5. Salt Precipitation

The effects of flooding do not stop at fluid-electrolyte infiltration into the GDL. The (bi)carbonates, dissolved in the electrolyte, can form carbonate salts with alkali cations, which accumulate near the cathode surface. The salts will then precipitate to solid crystals once the solubility limit is reached, either by water consumption or concentration increase. If formed or migrated to the already flooded GDL, the precipitates can permanently block the pores for gas transport. The lack of CO_2 at the reaction sites then shifts the dominant reaction to HER. Direct observation of salt was done by Disch et al [43], who performed neutron radiography to investigate water transport in a CO_2RR cell. They observed precipitated salts and precipitate-associated electrode flooding during the experiments, which explain the decrease in their cell's performance. Several experiments show that periodically washing the GDE can restore the cell's performance [16, 44].

The salts can move to the GDL through several ways. Hao et al [45], found that liquid droplets carrying salt can migrate from the cathode catalyst-membrane interface toward the back side of the GDE driven by interfacial gas evolution and CO_2 flow. Over time, the droplets dry out due to water consumption or CO_2 flow-induced evaporation, causing the salt to precipitate. Meanwhile, Joensen et al [46] add that the salts are carried by diffusion of water into the GDL due to the initially dry condition of the GDL.

2.6. Capillary Flow

In a CFE cell, a sheet of porous membrane is placed between the cell electrodes, with its bottom side dipped in an electrolyte reservoir. By assuming the pores to be pillars of cylindrical vertical channels, the liquid flow by capillary action can be approached by employing the Hagen-Poiseuille equation [11, 13]. This equation describes the flow rate Q of liquid flowing in a cylindrical pipe of constant cross-sectional area given a pressure drop of ΔP. As a pressure differential drives liquid flow, the pressure difference in this setup is the capillary pressure. A tortuosity (τ) term is added to account for the actual distance traveled by the liquid:

$$Q = \frac{n\pi r^4}{8\mu\tau}\frac{\Delta P}{L} \tag{2.18}$$

where n is the number of capillary channels with radius r, ΔP is the pressure drop, μ is the viscosity of the liquid, and L is the length of the channel (in this case, the height of the vertical membrane). The tortuosity τ can be approximated by using the membrane's porosity (ϵ) with the relation [47]:

$$\varepsilon = \frac{n\pi r^2}{A} \tag{2.19}$$

$$\tau = \frac{(2-\varepsilon)^2}{\varepsilon} \tag{2.20}$$

where r is the pore radius and A is the cross-sectional area of the porous membrane. By plugging in the capillary pressure P_C from equation (2.16), the fluid flow rate of a capillary membrane can be described as follows:

$$Q = \frac{\varepsilon^2 A r \gamma_{LG}\cos\theta}{4(2-\varepsilon)^2\mu L} \tag{2.21}$$

with γ_{GL} the gas-liquid surface tension and θ the contact angle of the electrolyte and membrane surface interface. For a completely hydrophilic membrane, the contact angle can be assumed to be zero. Thus, from the equation above, the capillary flow rate is shown to be proportional to the pore size of the membrane, the thickness of the membrane through the cross-sectional area A term, and the porosity of the membrane. Meanwhile, the flow rate decreases with the height of the column L. This relation places a limit to the scalability of capillary-fed cells because although the reactions involved in CO_2RR have no net water consumption, some amount of electrolyte is still needed to facilitate ion transport. Furthermore, the parasitic HER reaction, which requires water consumption, remains inevitable in the

current state of CO_2 electrolyzer technology. If water is depleted, salt concentration can rise beyond its solubility limit, precipitating and blocking mass transport.

3

Methodology

This chapter describes the setup used to obtain the experiment data. First, we explain the main components used in the CFE cell. Next, the connection between the cell and the supporting equipment that makes up the experiment setup is discussed. Finally, chronopotentiometry sequences used as the main electrochemical measurement method and the subsequent data processing are described.

3.1. Material

3.1.1. Electrode Catalyst

Anode

Owing to the still-superior Ir-based catalyst [48, 49], titanium substrate coated with IrO_2 catalyst (0.6 mg cm^{-2} loading) is used in this project. Titanium is commonly used as anode material for its stability in the harsh acidic environment and high anodic potential.

Cathode

The cathode GDE used in this project is based on Sigracet 39BB non-woven carbon paper purchased from Fuel Cell Store. It has a total thickness of 315 μm and the MPL is PTFE treated to 5 wt%. A catalyst ink based on silver nanopowder is sprayed-coated on the MPL side of the carbon paper with a target loading of 1.1 mg Ag cm^{-2}, forming the catalyst layer.

3.1.2. GDE Preparation

Sample Preparation

The carbon paper sample is cut to 20 cm x 6 cm and dried for 10 minutes at 120^oC. Then, the sample is weighed to obtain the weight before the catalyst depositing process. Next, the sample is placed on a metal plate with its position fixed. A mask is placed at the edges of the sample so the ink that will be sprayed on top of it will only deposit on the intended area.

Ink Preparation

The solid composition of the ink is determined to be 80 wt% AgNP and 20 wt% Nafion 521 ionomer. With a target loading of 1.1 mg Ag cm^{-2}, sample area of 100 cm^2, and an expected ink loss of 30%, we add 366.67 mg of Ag nanopowder (aerodynamic particle size (APS): 20-40 nm, 99.9%, Thermo Scientific), 36.63 mL of 1:1 mixture of water and isopropyl alcohol, and 1.969 mL of Nafion D-521 disperison (5 wt%, Alfa Aesar). The ink mixture is then homogenized in a sonication bath for at least 30 minutes before spraying process is started.

Deposition Process

The metal pad holding the sample is screwed on a custom made 2D-motorized stage. The airbrush, fed from the ink vial and a nitrogen line, is placed stationary a few centimeters from the sample to spray the ink continuously. The motorized stage then moves following a pre-determined path that ensures even spraying over the area of interest. At the back of the metal plate is a heating pad set at 130^oC to help evaporate the liquid phase of the ink. The

ink vial is continuously sonicated in the sonication bath to ensure homogeneity throughout the spraying process.

Post Process
After the vial is emptied from the ink, the now-sprayed sample is dried for 10 minutes at 120^oC before being weighed again to determine the catalyst loading. The sample is then cut to 2.2 cm x 2.2 cm pieces (approx. area of 5 cm^2) for use in the electrolysis cell.

3.1.3. PES Membrane
Polyether sulfone (PES) membrane is a porous, hydrophilic, membrane filters commonly used in clinical, life science, and general filtration purposes. Hodges et al [11] performed a survey of commercially available membranes for use as separator and found PES to have the lowest ionic resistance, with 80% porosity and contact angle of 70.3^o.

The PES membrane used in this project is purchased from Sterlitech [50], with available nominal pore sizes ranging from 0.03 to 8 μm and nominal thickness of 110-150 μm. In this project, we limit ourselves to only use PES with 1.2 μm, 5 μm, and 8 μm pore sizes. The bubble point, described as the gas pressure needed to pass through an already wetted membrane, for those sizes from the manufacturer's datasheet are 896 mbar, 758 mbar, and 413 mbar, respectively.

3.1.4. Electrolyte
In the theoretical background section, the importance of alkali cation presence and the benefit of larger cations have been elaborated. For that reason, $CsHCO_3$ electrolyte (Thermofisher Scientific, 99.99%) is used in this project. The bicarbonate (HCO_3^-) anion is selected to provide the alkaline environment known to promote CO_2RR.

3.2. Experimental Setup
Capillary-Fed Electrolysis Cell
Figure 3.1 shows the construction of the CFE cell. The steel backplate measures 7.5 x 7.5 cm^2 and features a serpentine flow channel with inlet/outlet nozzles on the opposite side. The anode backplate has a similar construction and is made of titanium. The CFE cell employs a zero-gap architecture where the electrodes and separator membrane are pressed together, leaving no gap. The cathode is placed with the catalyst layer facing the PES membrane. PTFE gaskets are used to insulate the two plates electrically and to prevent gas and liquid leaks. Gasket thicknesses are chosen to be slightly thinner than the electrodes to ensure the electrodes are in contact with the metal backplates and to avoid high contact resistance. In our setup, the anode thickness is ~280 μm, and the anode side gasket thickness is ~270 μm.

Meanwhile, the cathode has a thickness of ~320 μm with a cathode gasket thickness of ~260 μm. The PES membrane is cut with an extra 2 cm at the bottom so it can be dipped into an electrolyte reservoir. The cell is then bolted with a torque of 2 Nm, complete with a set of insulating bushings to prevent electrical contact. However, the bottom-middle bolt hole is not bolted to prevent obstruction of the capillary flow in the PES membrane.

The assembled cell is then connected to the gas lines and the potentiostat (Ivium XP20) in a 4-electrode setup as illustrated in Figure 3.2. The CO_2 feed gas is passed through two humidifier columns to reach 100% relative humidity. A bypass valve can be switched to allow CO_2 gas to immediately flow into the cell if a dry feed is desired. CO_2 gas enters the cell via the top nozzle, and the cathodic gas product along with the unreacted CO_2 exits via the bottom nozzle. This flow direction allows downward exit of condensed water and liquid product, preventing them from becoming trapped in the cathode flow channel. Since we are interested in the composition of the gas product, the cathode outlet is channeled to a gas chromatograph (Global Analyser Solutions CompactGC 4.0). A liquid trap bottle is placed immediately after the cell exit to prevent condensate from entering the GC.

Meanwhile, mass flow meters (MFMs, from Bronkhorst) measure the pressure and flow rate upstream and downstream of the cell. The cell is held in an elevated position by two clamps to

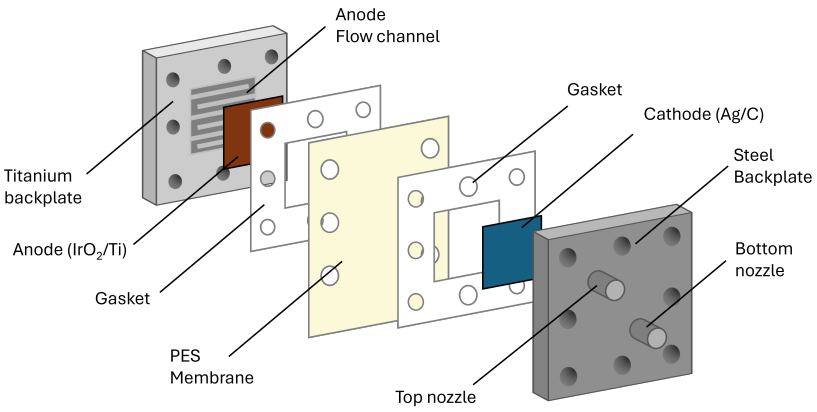

Figure 3.1: Exploded view of the CFE cell construction.

allow the placement of a petri dish containing the electrolyte liquid beneath it (see Supporting Information A.1). Thermocouples are also inserted into the available slot at the top of the cathode and anode backplates to measure the internal cell temperature.

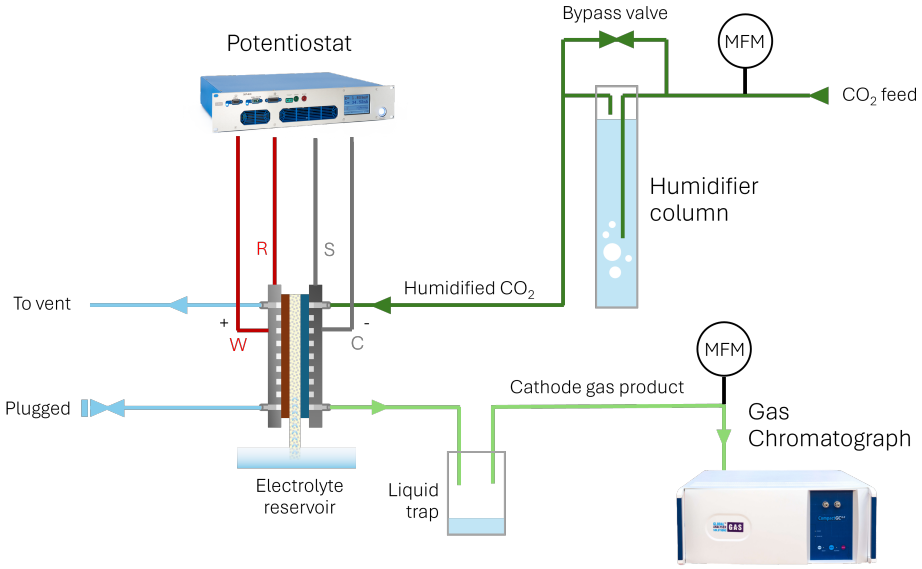

Figure 3.2: Experiment setup with a CFE cell.

In one experiment, we fed 80%-humidified CO_2 despite the humidifier column only feeding either completely dry or completely humidified CO_2. To accomplish this, a second CO_2 feed line, which is not connected to the humidifier column, is used. A T-line connector is then installed to combine the flow from the two lines. By configuring the flow rate from each line, any percentage of humidification in the combined CO_2 flow can be achieved.

Conventional Anolyte-Flow Electrolysis Cell

The conventional anolyte-flow cell used for comparison with the CFE cell studied has a very similar construction, with the only difference being an AEM (PiperION, 40 μm, purchased from the Fuelcell store) positioned in place of the PES membrane. With an anolyte flow, the setup now includes a peristaltic pump (Masterflex L/S), set at 30 rpm, and the anolyte line as illustrated in Figure 3.3. The electrolyte is 0.5 M $CsHCO_3$ with a volume of 40 mL placed in a glass reservoir.

In contrast to the flow direction of the CO_2 feed gas, the anolyte liquid is fed from the bottom

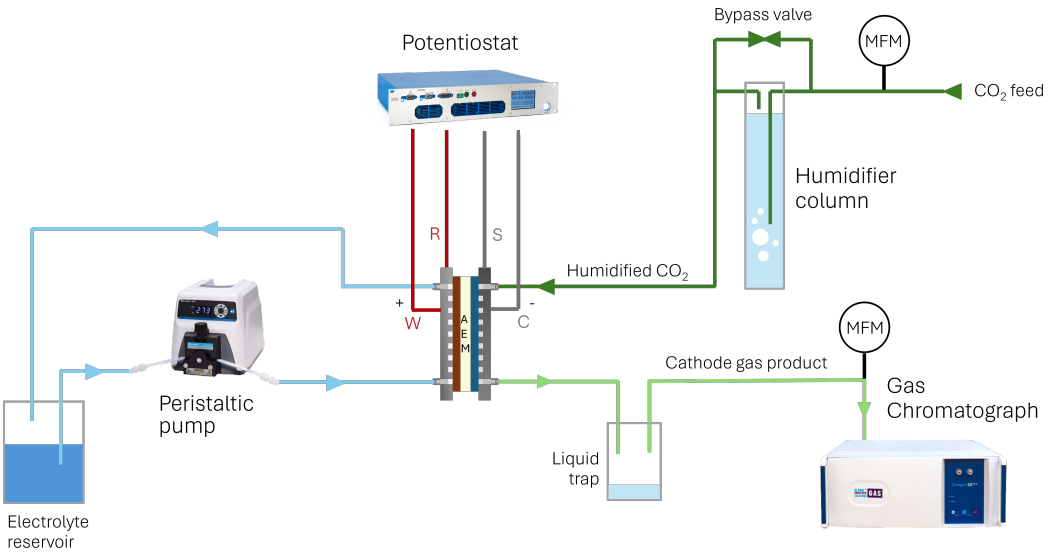

Figure 3.3: Experiment setup with a conventional anolyte-flow cell

nozzle of the anode backplate. It exits at the top to allow anodic gas products to exit the cell easily upward.

3.3. Electrochemical Experiment

Chronopotentiometry is used extensively in this study since we are interested in the required potential at different applied current densities of a CFE cell. The experiments are divided into two types: short-term and long-term.

Short-term experiments are performed primarily to examine the behavior, mainly the voltage evolution and Faradaic efficiency, of a configuration being tested. However, due to the occurrence of the initial voltage peak, which could take several hours to stabilize, a conditioning phase is performed to let the voltage stabilize enough. This phase is limited to two hours due to time constraints. Therefore, the chronopotentiometry run would then consist of 2 hours of conditioning with 50 mA/cm^2, continued by a sequence of 100 mA/cm^2, 200 mA/cm^2, and back to 100 mA/cm^2 with 40 minutes each. The last 100 mA/cm^2 runs are performed to observe the behavior of the system going from a higher current density. During the experiment, both voltage and current are recorded by the potentiostat, while the gas product is injected for GC analysis every 4 minutes.

Finally, longer-term chronopotentiometry experiments are conducted to assess the cell's performance stability under the given conditions. For these longer term experiments, standardized chronopotentiometry sequence comprising of 50 mA/cm^2, 100 mA/cm^2, 150 mA/cm^2, 200 mA/cm^2, 150 mA/cm^2, each lasting 4 hours and continues with a last bit of 100 mA/cm^2 for 2 hours is used. The total run is 22 hours. For experiments with 0.1 M electrolyte concentration, due to the very high initial voltage peak (reaching above 10 V, which is above the voltage range of the potentiostat) if the applied current starts immediately from 50 mA/cm^2, we ramp the current from 0 to 50 mA/cm^2 with a rate of 0.1 mA/s. Slowly ramping the applied current, rather than a step-increase to 50 mA/cm^2, has been tried and shown to reduce the peak height. This effect can be attributed to the slower buildup of the ion gradient, resulting in less aggressive initial CO_2 bubble formation.

3.4. Data Processing

Voltage Measurement

Since the voltage during the initial stage of the experiment is elevated and unstable due to the

initial voltage peak, voltage data are obtained from the long-term experiments after the initial voltage peak has subsided. For that reason, only the voltages of the last three applied current densities (200 mA/cm^2, 150 mA/cm^2, and 100 mA/cm^2) can be reliably reported, which is taken as the average of the last 75% of the duration of a given applied current density.

Faradaic Efficiency Calculation

Faradaic efficiency is calculated by the output of the GC in combination with the flow rate measurement by the downstream MFM. For every injection, the GC outputs the mole fraction of the gas species it is configured to detect, comprising oxygen, nitrogen, carbon monoxide, carbon dioxide, and hydrogen gas. These values are then normalized.

The MFM measures gas flow rate by its thermal and other physical properties and is calibrated to CO_2. Therefore, a different mix of gas will require a correction factor to calculate the actual flow rate from the measured flow rate. The correction factor is calculated from the composition of the gas and the component-specific conversion factor provided by the manufacturer (Bronkhorst) by the following expression:

$$\frac{1}{CF} = \sum_i \frac{y_i}{k_i} \tag{3.1}$$

where y_i is the mole fraction of the gas species i detected by the GC and k_i is the conversion factor for that gas species. The corrected flow rate Q_{corr} can then be calculated by multiplying the measured flow rate Q_{meas} by the correction factor CF. In this study, the measured flow rate is taken from the average flow rates in the last 10 seconds before the GC injection.

$$Q_{corr} = Q_{meas} \times CF \tag{3.2}$$

With the true flow rate of the outlet gas known, the partial flow rate of CO is simply obtained by multiplying the outlet gas flow rate by the mole fraction of CO species given by the GC. Since the MFM reports the flow rate data in standard conditions, the mole rate of CO gas $\dot{n}_{CO}$ can be calculated by dividing the partial CO flow rate by the standard molar volume of ideal gas $V_m^o = 22.4\text{L/mol}$.

$$\dot{n}_{CO} = \frac{Q_{corr} \times y_{CO}}{V_m^o} \tag{3.3}$$

where y_{CO} is the mole fraction of CO given by the GC. Finally, the faradaic efficiency for CO FE_{CO} can be calculated by taking the ratio of the partial current of CO over the total current.

$$FE_{CO} = \frac{zF\dot{n}_{CO}}{I} \tag{3.4}$$

where z is the mole of electron participating per mole produced CO, F is faraday constant 96485 C/mol, and I is the applied current.

Energy Consumption Calculation

The energy consumption (kWh/mol CO) can be calculated using the formula below:

$$\text{Energy consumption}\left(\frac{\text{kWh}}{\text{mol CO}}\right) = \frac{\text{Voltage}_{\text{cell}} \times \text{current} \times \text{Time}}{\text{Moles of CO produced}}$$

4

Results and Discussion

In this chapter, the results and discussion of the performed experiments are elaborated. The discussion begins with the observation of the initial voltage peak that occurs in every of our CO_2RR experiments. The hypothesis that the voltage peak is caused by trapped CO_2 bubbles and the proofs supporting the hypothesis will be presented, followed by a proposed mechanism on how CO_2 bubble blockages can induce the voltage rise. The longer-term stability of an operating CFE cell is then evaluated under different operating parameters. The results suggest that water management and salt precipitation are the most important aspects for stable CFE cell operation. The chapter concludes with a discussion on the performance comparison between the proposed CFE cell and a hybrid-MEA cell constructed with identical components for a fair comparison.

4.1. Observation of The Initial Voltage Peak

When we perform a chronopotentiometry run at 50 mA/cm^2 and hold it for a few hours, a pattern of high initial voltage, as shown in Figure 4.1, is observed. This initial increase in voltage takes a few minutes to reach the peak height and then slowly dissipates on the scale of a few hours.

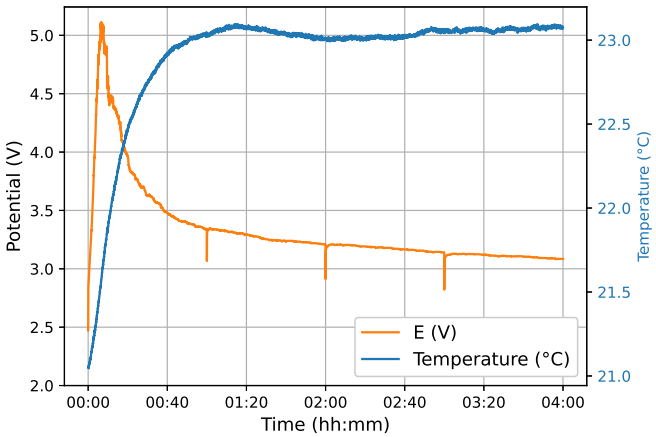

Figure 4.1: Initial high voltage peak and the temperature measurement in experiment with 0.5M $CsHCO_3$ electrolyte and 50 mA/cm^2 applied current density. The sharp dips are pauses from current interrupt measurements.

Temperature measurement using thermocouples inserted into the available slot in the cell's backplate shows that the temperature rises from the ambient lab temperature of 21^oC to only 23^oC. The paper by Hurkman et al [51] shows in their simulation that an increase in operating

temperature from 20^oC to 80^oC in 50 mA/cm^2 barely reduces the applied potential. Since in our experiment the potential drops by 2 V after the peak, we conclude that temperature cannot be the dominant factor.

To rule out the role of impurities in the membrane, we soaked the PES membrane in DI water or in an HCl solution. The attempt did not result in any observable reduction in the voltage peak. We then reused the PES membrane from a previous experiment, in which we ran the cell until the voltage peak stabilized. If the voltage peak is caused by a physical or chemical property of the PES, then reusing a PES that has stabilized at a voltage is expected not to cause another high-voltage peak. However, a reused PES still yields an initial high-voltage peak. We then acquired a higher-grade $CsHCO_3$ salt in case the impurities originated from the salt used. Similarly, an initial high voltage peak is still observed.

Another possible cause of the increased voltage is incomplete filling of the membrane pores with electrolyte, as unfilled pores from trapped gas can block ion transport. However, pre-soaking the PES membrane in 0.5 M $CsHCO_3$ electrolyte solution overnight also did not eliminate the initial voltage increase.

Further experiments found that the magnitude of the initial voltage peak is strongly affected by the electrolyte concentration. As shown in Figure 4.2a below, lower electrolyte concentration increases the height of the initial voltage. At a 0.1 M $CsHCO_3$ concentration, the voltage exceeded 10 V, which is above the maximum voltage the potentiostat can record. By comparing the onset, we also observe that the voltage peak reaches its maximum height more quickly with lower electrolyte concentration.

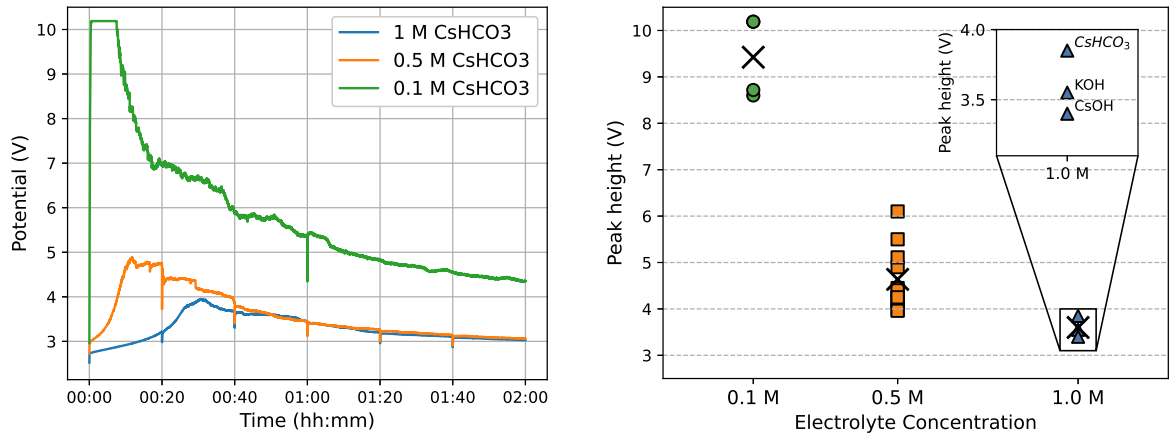

Figure 4.2: (a) Initial voltage height comparison with 50 mA/cm^2 applied current in 0.1 M, 0.5 M, and 1 M $CsHCO_3$ electrolyte concentrations. (b) Distribution of peak heights over several experiments in different electrolyte concentrations with 50 mA/cm^2 applied current and 5 μm membrane pore size. The "X" marks the average data point.

The height of the initial voltage peak, even under similar conditions, is not always the same. Figure 4.2b shows the initial peak heights observed across several experiments at electrolyte concentrations of 0.1 M, 0.5 M, and 1 M. Despite the wide range of peak heights an experiment could have, the distribution confirms that the peak heights increase with lower electrolyte concentration. For experiments in 0.1 M $CsHCO_3$ electrolyte, the actual average voltage height may be higher than the marked value in the plot, since the topmost data point represents the highest voltage the potentiostat can record rather than the actual voltage. Meanwhile, each of the three data points in the 1 M concentration experiments used different salts as annotated in the inset plot, indicating that the initial voltage peak is present not only with $CsHCO_3$ but also KOH and CsOH electrolytes.

The maximum height of the initial voltage peak also increases when a PES membrane with a smaller pore size is used. Shown in Figure 4.3, the experiment using a 1.2 μm PES pore

size exhibits a much higher initial voltage peak compared to using a 5 μm pore membrane, reaching 8 V, which is the upper voltage limit set as a safety feature for the potentiostat. The initial voltage peak then recedes and stabilizes at a voltage similar to that in the 5 μm PES pore-size experiment. However, we did not observe a significant difference in potential when comparing a CFE cell with 5 μm and 8 μm pore size. A plot of the peak height distribution is shown in Supporting Information A.2.

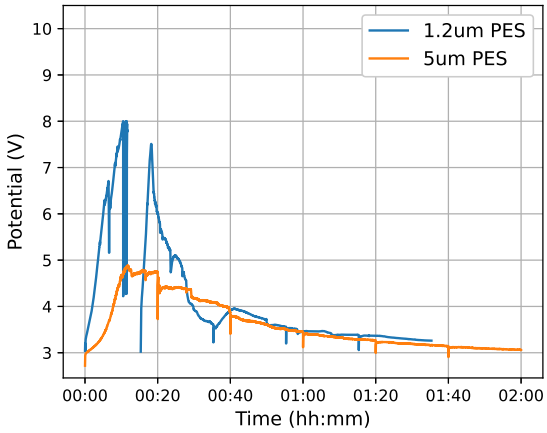

Figure 4.3: Initial voltage height comparison with 50 mA/cm^2 applied current in 1.2 μm and 5 μm PES pore sizes in 0.5 M $CsHCO_3$.

Our experiments also show that the onset of the initial voltage peak is dependent on the applied current. Figure 4.4 shows the voltage evolution in experiments with applied current densities of 50 mA/cm^2, 100 mA/cm^2, and 200 mA/cm^2. With higher applied current, a faster increase in voltage is observed. As can be seen in the figure, the voltage of the 200 mA/cm^2 experiment goes immediately high and reaches the peak within 5 minutes of current start, while the voltage in the 50 mA/cm^2 experiment took about 30 minutes to reach the highest peak. Such an increase in the steepness of the voltage rise is also observable in the previously discussed effect of electrolyte concentration, which results in a higher maximum voltage. However, the effect of different applied currents on the maximum voltage height is less clear.

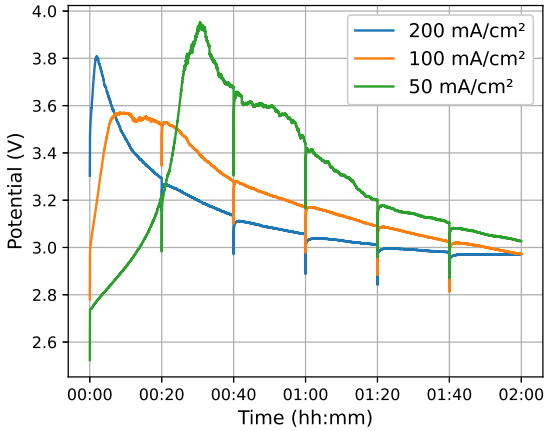

Figure 4.4: Initial voltage height comparison with 50 mA/cm^2, 100 mA/cm^2, and 200 mA/cm^2 applied current densities in 1 M $CsHCO_3$.

Considering that the voltage peak maximum height follows a distribution instead of being the same at every repeated experiment, the lower peak height of the 100 mA/cm^2 shown

in the last figure cannot be interpreted as a trend, since it could simply be that, for that particular experiment, the peak height falls at the lower end of its distribution. Therefore, the relationship between the voltage peak height and the applied current density cannot be determined from this comparison alone. More experimental data is required to uncover whether a relationship exists.

4.2. Initial Voltage Peak Mechanism

4.2.1. CO_2 Bubble Hypothesis

CFE uses a porous membrane that transports ions nonselectively. This non-selectivity allows the acidic environment due to the anodic half-reaction to extend into the electrolyte-filled porous membrane. Meanwhile, (bi)carbonate anions are produced on the cathode side by OH^- and the CO_2 feed reaction and will then be transported to the anode side by diffusion and drift through the membrane. The low-pH gradient near the anode then shifts the equilibrium (bi)carbonate back to dissolved CO_2. However, due to low solubility, supersaturated dissolved CO_2 will form gas bubbles within the membrane pore matrix, which could block the membrane as they grow. Figure 4.5 illustrates the hypothesized mechanism. This blockage inhibits the ionic transport necessary to complete the circuit. A larger voltage is then needed to drive the reaction rate at the set applied current. As bubbles begin to dissolve over time as the supersaturation recedes and an equilibrium flow is established, the voltage slowly stabilizes. Although (bi)carbonate degassing to CO_2 also occurs in an alkaline conventional cell using an anion-exchange membrane, the membrane's charge selectivity prevents a pH gradient from developing within it. Thus, degassing can occur only at the membrane-anode interface, outside the membrane itself. In another study using a porous membrane and acidic electrolyte, Wei et al [15] provided no report on bubble-induced voltage increase, which could be explained by the much lower crossover of (bi)carbonate in acidic electrolyte in the first place.

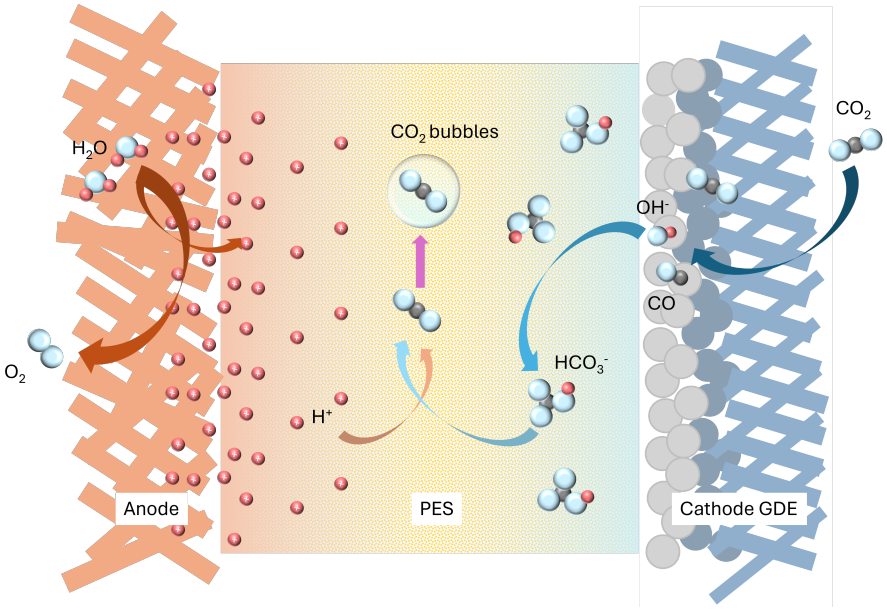

Figure 4.5: Illustration of CO_2 gas bubble formation inside the porous membrane.

4.2.2. Proof that The Initial Voltage Peak is Caused by Trapped CO_2 Bubbles

To prove that (bi)carbonate degassing to CO_2 bubbles is the cause of the voltage increase, we can design experiments that prevent such reactions from happening by either removing the (bi)carbonate source or by displacing the neutralization reaction to outside the membrane, where the formed CO_2 bubbles will not get trapped.

Absence of initial voltage peak in water electrolysis with CsOH electrolyte
In this experiment, CsOH electrolyte is used instead of $CsHCO_3$, and the CO_2 feed flow is shut off to eliminate any source of DIC. In the absence of CO_2, the cathode will fully perform HER instead. The OH^- will migrate to the anode side and act as a reactant for the anodic OER. With no carbonic species present, no gas-forming reaction will occur, which would manifest as the absence of gas bubbles that could disrupt ion transport and increase the voltage. As shown in the figure 4.6 below with the orange line, we observe the voltage evolution to be a flat, stable line, confirming our prediction.

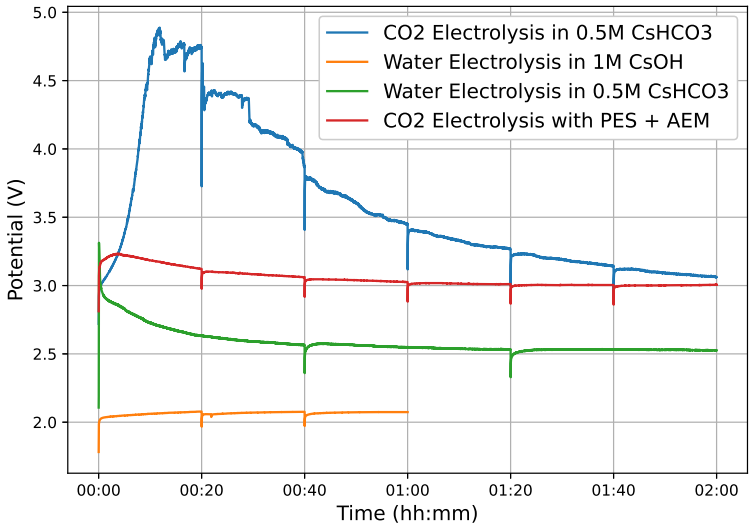

Figure 4.6: The initial voltage of CO_2 electrolysis in 0.5M $CsHCO_3$ (50 mA/cm^2) [blue] compared against: water electrolysis in 1M CsOH electrolyte (50 mA/cm^2) [orange], water electrolysis in 0.5M $CsHCO_3$ electrolyte (100 mA/cm^2) [green], and CO_2 electrolysis with AEM sandwiched between anode and PES membrane (50 mA/cm^2) [red].

Smaller and shorter voltage peak in water electrolysis with $CsHCO_3$ electrolyte
In another experiment, $CsHCO_3$ electrolyte is used while the CO_2 feed is still kept shut off. The amount of DIC present in the system is now constrained to the amount already contained in the small volume of the electrolyte inside the cell. Upon current flow and (bi)carbonate neutralization by anode acidification, the DIC present in the electrolyte reservoir at the bottom of the cell is unlikely to diffuse up the capillary columns of the membrane to replenish the spent (bi)carbonates. Ionic transport from the electrolyte reservoir is governed only by diffusion and convection of the bulk solution. For diffusion, the time t it takes for an ion to travel a distance L can be calculated by:

$$t = \frac{L^2}{D} \tag{4.1}$$

where D is the diffusion coefficient of the ion. With bicarbonate having a diffusion coefficient of $1.18 \times 10^{-9} m^2/s$ [52], the time it takes the bicarbonate ions to travel 4 cm upward is in the order of days. This slow diffusion practically isolates a CFE cell from its own electrolyte reservoir on the time scale relevant to the typical duration of an experiment. Other ways in which the ions inside the cell can be replenished are by convection of the bulk electrolyte, which requires that water be consumed at the other end. Since evaporation is expected to be negligible given the tight gap of the cell assembly, HER will be the dominant water-loss mechanism from the system, which is itself too slow to drive adequate bicarbonate replenishment.

Our prediction is proven, as shown in Figure 4.6 with the green line. When the current is applied, the voltage rises sharply, drops almost immediately, then follows a tail that stabilizes. The smaller voltage peak can be explained by CO_2 degassing from the (bi)carbonates already

present in the cell volume. The subsequent quick dissipation is caused by the absence of CO_2 feed flow that sustains the (bi)carbonate regeneration.

Absence of initial voltage peak in CO_2 electrolysis if AEM is placed on the anode side An AEM, which only allows anions to pass and blocks cations, is placed between the PES membrane and the anode, as illustrated in Figure 4.7. Just like in a conventional cell employing an AEM, the (bi)carbonate neutralization by the acidified anode will only occur at the anode-AEM interface, outside the PES membrane, where it can no longer get stuck and block ion transport. As can be observed in Figure 4.6 with the red line, this configuration also yields no initial high voltage peak, as expected. A much smaller initial voltage bulge is observed, which can be explained by the concentration gradients still establishing within the AEM when current is initially applied.

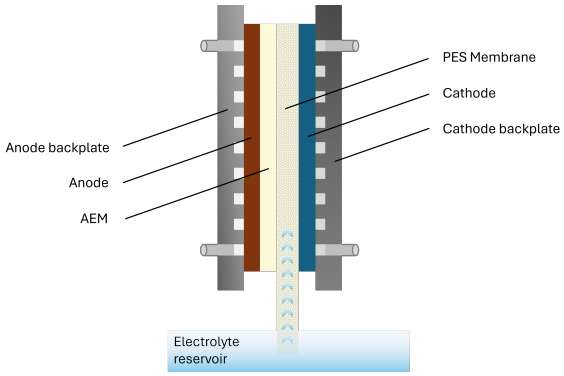

Figure 4.7: Illustration of AEM sandwiched between anode and PES membrane in the CFE cell.

4.3. Proposed Mechanism of How the CO_2 Bubble Blockages Increases Voltage

The presence of bubbles can reduce the effective electrolyte conductivity by reducing the number of pathways available for ionic migration [53], increasing the ohmic overpotential. The presence of bubbles can be quantified by the void fraction. The void fraction (ϵ) then changes the effective conductivity (κ) by Bruggemann's relation below:

$$\kappa = \kappa_o(1-\epsilon)^{3/2} \tag{4.2}$$

This relationship explains the much higher initial voltage peak when a lower-concentration electrolyte is used, since it has lower initial conductivity (κ_o).

Membrane pore size also affects how easily the bubbles can dislodge, with smaller pores making bubbles harder to escape [54, 55]. This pore-size influence explains why the experiment with the smaller 1.2 μm membrane also exhibits a higher initial voltage peak compared to the 5 μm membrane. The longer residence time of the bubbles increases the overall void fraction of the electrolyte, thereby reducing the effective conductivity. In addition, we find that the cathode may also affect the initial voltage peak.

Shown in Figure 4.8, when an experiment is performed with a reused cathode from a previous experiment, the initial voltage peak is significantly lower. The same effect is not observed when the anode is reused, as the voltage evolution shows a height comparable to that of an experiment with new electrodes. This difference could indicate a change in the cathode's physical properties that contributes to the initial voltage peak.

We gather that there are at least two changes in the cathode after an experiment: reduced thickness and reduced hydrophobicity.

The thickness reduction originates from the thinner gasket we place on the cathode side to ensure good contact from the compression. Since the combined gasket thickness used is ~260 μm while the cathode GDE thickness is ~320 μm, the flow channel is pressed into the

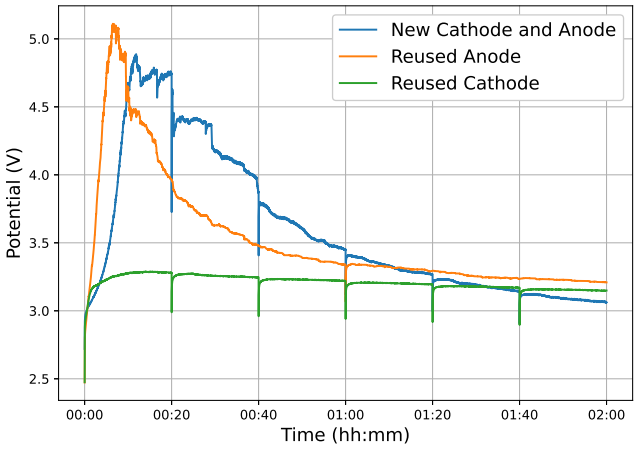

Figure 4.8: Initial voltage peak in experiment with reused electrodes in 0.5M $CsHCO_3$ and 50 mA/cm^2 applied current density.

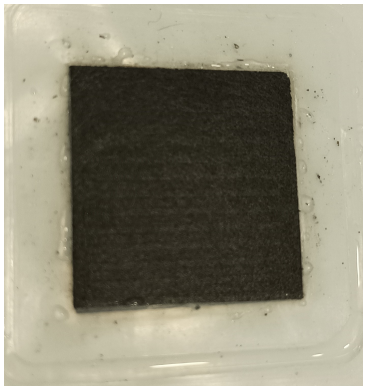

Figure 4.9: Impression of the serpentine flow channel on the cathode carbon substrate.

backside of the cathode GDE, leaving a visible impression of the serpentine flow channel pattern on the brittle carbon substrate shown in Figure 4.9. When the cathode is reused, the compression on the cathode by the metal plate would be less, since the back side of the cathode that contacts the flow channel is already dented from previous use. This reduced compression might allow a gap to form between the cathode and the PES membrane interface, which provides an escape route for the CO_2 bubbles and thereby reduces the bubble residence time. There are reports where adding a small gap between the electrode and the separator, thus deviating from a true zero-gap, can lower the overpotential by providing sufficient space to prevent gas bubble accumulation [56, 57]. Our data on the voltage peak heights in experiments with lower bolt compression, which would produce a similar effect, do not yet provide a conclusive conclusion (See Supporting Information A.2).

Another possible change is an irreversible decrease in hydrophobicity due to PTFE degradation at more negative overpotentials [58]. There are reports of contact angle measurements showing reduced contact angle after a cathode is used in electrolysis [44, 59], indicating reduced hydrophobicity. A similar phenomenon may be occurring with our cathode. Lower hydrophobicity is known to decrease bubble adhesion effectiveness, making them easier to detach. This property applies not only to bubbles nucleating from a surface as in the case of the formation of gas product on an electrode surface [60, 61], but also to bubbles that form elsewhere that approach a surface and then attach to it [62, 63]. The reduced hydrophobicity helps bubbles approaching and attaching to the cathode surface detach more quickly and return to the bulk, thereby reducing their residence time near the surface.

Therefore, it is hypothesized that the absence of an interfacial gap or the high hydrophobicity of the cathode surface causes the bubbles formed to accumulate on the cathode surface. As reported in several works, bubbles adhering to the cathode surface will cover a fraction of the active area and make it inactive. This partial insulation creates a locally high current density in the uncovered areas and, by the Butler-Volmer relation, increases the kinetic overpotential [64, 65, 66].

The locally increased reaction rates might explain the observed dip in Faradaic efficiency to CO, whose timing coincides with the peak and then recovers just as the voltage stabilizes. Examples of such effects can be seen in Figure 4.10a below.

As areas of high reaction rates emerge, the CO_2(aq) reactant could be depleted due to mass-transport limitations, thereby shifting some of the Faradaic current to HER. Then, as the bubbles slowly dissipate, the applied current returns to a more even distribution and CO_2 concentration at the reaction site recovers, so FE_{CO} also recovers.

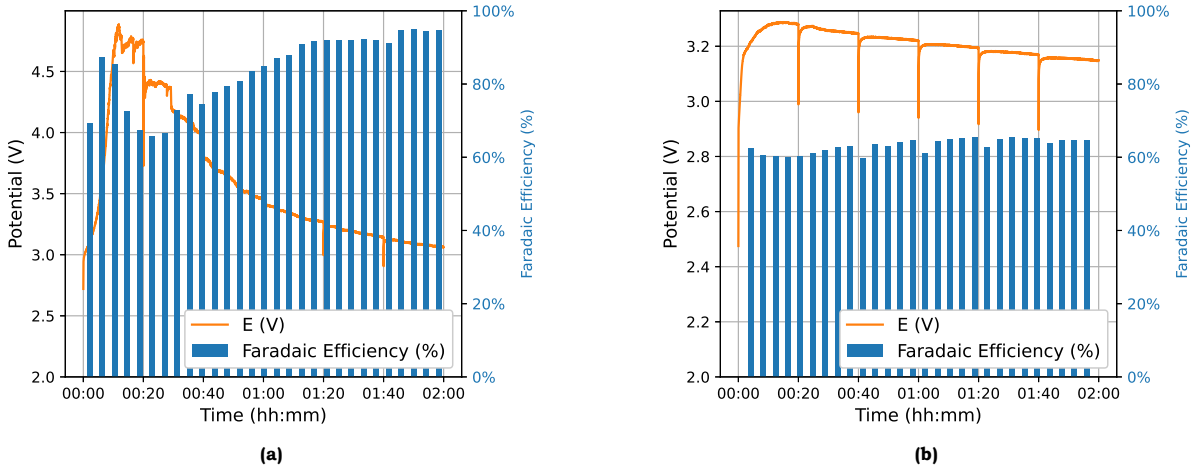

Figure 4.10: (a) Dip of FE_{CO} coinciding with the voltage peak in the experiment with 0.5 M $CsHCO_3$ and (b) the experiment with reused cathode shows no apparent dip in FE_{CO}.

The faradaic efficiency evolution of the reused cathode experiment is shown in Figure 4.10b, which shows that the dip in FE_{CO} is not as apparent as in pristine cathode experiments. This observation supports the understanding that the process causing the initial high peak also temporarily lowers FE_{CO}. However, what causes the effect to be less apparent in a reused cathode, whether it is due to the increased interfacial gap owing to lower compression or the reduced hydrophobicity of the cathode surface, cannot yet be determined and requires further research. The suggested experimental pathway will be elaborated further in Chapter 6 (Recommendations for future work).

In conclusion, our working theory for the initial voltage peak is that it is the combined effect of increased electrolyte ohmic potential and increased kinetic overpotential of the cathodic reaction. Both result from bubbles that have stuck within the membrane pore matrix and in the vicinity of the cathode surface.

4.4. CFE Under Different Operating Parameters

Longer-time-scale experiments were performed to study the effect of different parameters on the operating stability of the CFE cell. The parameters to be varied are the bolt compression of the cell assembly, the electrolyte concentration, and the humidification of the feed CO_2 gas, to assess their effects on water management [67]. For that purpose, a set of experiments is compared to extract the trend, with FE_{CO} and salt precipitation as the metrics of interest. Salt precipitation can be inferred by the effect a salt blockage has on the upstream pressure of the CO_2 feed gas. The presence of salt blockage will increase the pressure reading up to a maximum of 2.8 bar, which is the head pressure of the CO_2 feed line. If the upstream pressure reaches its maximum, it means the CO_2 feed gas can no longer flow into the cell, and the cell is said to have catastrophic salt blockage.

4.4.1. Cell Compression

Cell compression can be adjusted by applying torque to the bolts that hold the cell. First, we examine the effect of applying 2 Nm and 1 Nm torque in 0.5 M $CsHCO_3$ electrolyte concentration. Figure 4.11 plots the evolution of faradaic efficiency for CO product during the course of the experiment with GC injection rate taken every 4 minutes. The figure shows that the experiment with 2 Nm compression (blue line) shows slightly higher FE_{CO} with a widening gap, although it then gets completely blocked by salt after 14 hours. Meanwhile, the 1 Nm experiment continues with lower FE_{CO}, which stabilizes at 200 mA/cm^2 (purple region), until the end of the experiment duration without catastrophic blockage.

The higher FE_{CO} in the 2 Nm experiment might be due to the lower capillary flow rate, resulting in less water surplus that could contribute to cathode flooding. Measuring the PES

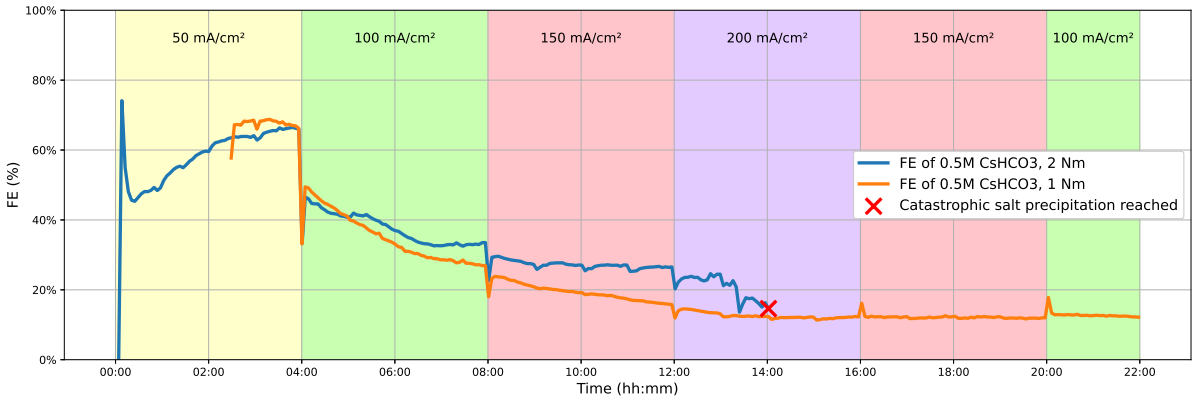

Figure 4.11: FE_{CO} over time of the 2 Nm and 1 Nm-compressed CFE cell in 0.5 M $CsHCO_3$. The 1 Nm experiment data did not start at time = 0 because there was a leak in the line connecting the cell to the GC. The small spikes and dips in FE_{CO} when transitioning to a different applied current are because the gas product has to fill up the liquid trap bottle first before continuing to the GC, and a stable gas mixture corresponding to the applied current has not been reached.

membrane thickness before and after the experiment reveals that the originally ~130 μm thick membrane is compressed to ~120 μm and ~100 μm for 1 Nm and 2 Nm, respectively. Applying equation 2.21 for capillary flow rate and accounting for the porosity change, we estimate that a 1 Nm-compressed CFE cell delivers 44.19% more flow rate compared to the 2 Nm (see Supporting Information A.3 for flow rate model). The increased flow could then flood the cathode more, lowering the CO product selectivity.

The catastrophic salt blockage occurring in the experiment with 2 Nm compression is confirmed upon disassembly of the cell. Figure 4.12 shows the catastrophic salt deposits formed in the experiment with 2 Nm bolt compression, which completely block the upper rows of the cathode flow channel. We found that such salt formation in the CFE cell tends to form in the upper rows of the flow channel. This finding can also be explained by the lower capillary flow rate, which decreases with height. The capillary flow rate at a given point is then further reduced by water consumption in the active regions beneath it. Thus, in locations with less water supply, salts can more quickly reach supersaturation and precipitate.

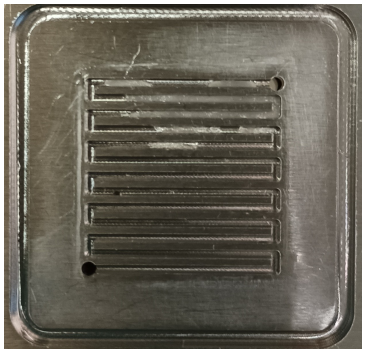

Figure 4.12: Heavy salt precipitation in the upper rows of the cathode flow channel in the experiment with 2 Nm bolt compression.

Meanwhile, we did not find any visible salt deposits in the flow channel of the experiment with 1 Nm cell compression. Thus, although the less-compressed cell appears to be flooded more and therefore has worse FE_{CO} performance as indicated in the experiment with 1 Nm cell compression, the more abundant water supply seems to delay salt supersaturation and, subsequently, the formation of catastrophic precipitates.

The finding of higher FE_{CO} in a more compressed membrane is supported by a similar conclusion from an experiment with the CO_2 feed gas fed from the bottom nozzle of the cell,

shown in Supporting Information A.4. Feeding CO_2 from the bottom nozzle bypasses the salt precipitates that form on the top rows of the serpentine flow channel. Without the feed gas ever being completely blocked, the more compressed cell exhibits higher FE_{CO} over the course of the experiment.

A similar conclusion can also be drawn from the same comparison in 0.1 M electrolyte concentration shown in Figure 4.13. At 0.1 M electrolyte concentration, salt precipitation appears reduced, as indicated by the absence of catastrophic salt precipitation. In this configuration, the 2 Nm experiment also shows slightly higher FE_{CO} compared to the 1 Nm up to the end of the experiment.

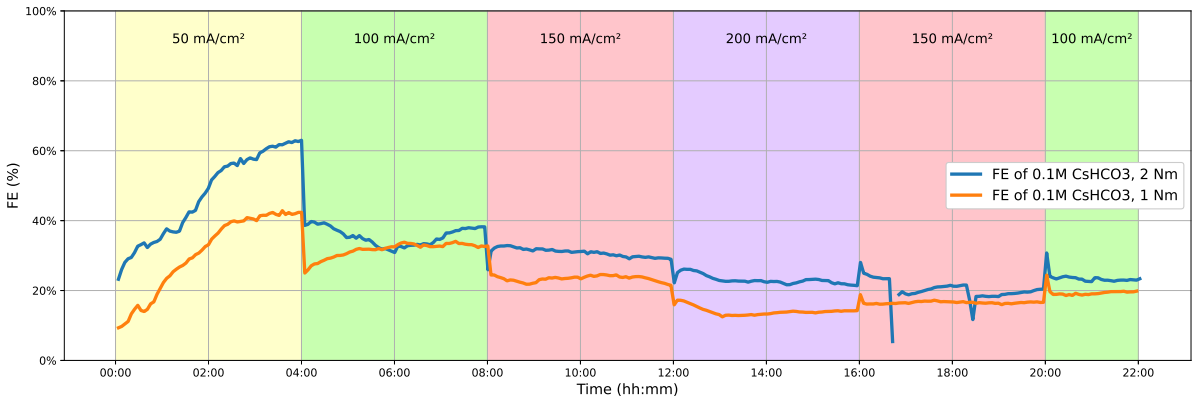

Figure 4.13: FE_{CO} over time of the 2Nm and 1Nm-compressed CFE cell in 0.1M $CsHCO_3$.

The relationship between water supply and salt precipitation can also be observed in experiments comparing PES membranes with different pore sizes. Again, applying equation 2.21 for the capillary flow rate, a membrane with a 1.2 μm pore diameter can only deliver 24% of the flow rate of a membrane with a 5 μm pore diameter (see Supporting Information A.3 for the flow rate model). This effect explains the low FE_{CO} of the experiment with 1.2 μm pores compared to 5 μm, which averages to 35% and 80% respectively at 50 mA/cm^2 applied current density. Since less water is delivered, water can reach depletion more quickly and inevitably precipitate salt more quickly. These results not only show the importance of water management in a CFE cell but also show how proper pore-size selection and cell compression can be used to control the water supply.

4.4.2. Electrolyte Concentrations

Comparison of CFE cell voltages with 0.1 M, 0.5 M, and 1 M electrolyte concentrations shows an expected trend. As shown in Figure 4.14, a higher electrolyte concentration lowers the voltage required to operate the cell at a given applied current. This effect can be explained simply by the higher ionic conductivity of the electrolyte.

In addition to voltages, different electrolyte concentrations also affect the probability of catastrophic salt precipitation occurrence. This effect can be observed by comparing experiments with electrolyte concentrations of 0.1 M and 0.5 M. Two sets of comparisons are performed, one with 1 Nm bolt torque and the other with 2 Nm.

First, we compare the performance of the two concentrations in a 2 Nm-compressed cell. As shown in Figure 4.15, the 0.5 M electrolyte concentration experiment reaches catastrophic salt precipitation after 14 hours, while the 0.1 M electrolyte concentration experiment continued. Gyenes et al [68] suggested that a 0.5 M concentration of $CsHCO_3$ electrolyte sits at the "sweet spot" of Cs^+ amount, yielding maximum FE_{CO}, while 0.1 M is shown to be insufficient. Their observation might explain the initially higher FE_{CO} in the 0.5 M experiment, as seen during the 50 mA/cm^2 current-density phase (yellow region). As the experiment progresses, the advantage of having a higher Cs^+ concentration is counterbalanced by increasing salt precipitation, thereby worsening performance. As shown in the figure, the orange line rep-

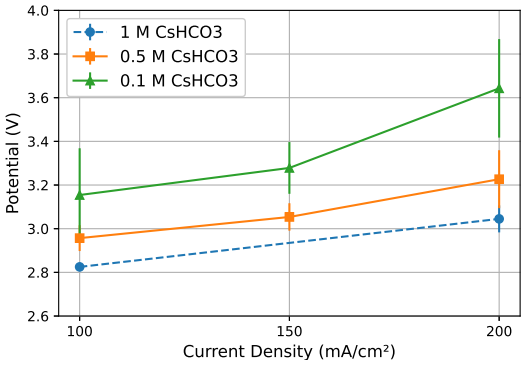

Figure 4.14: The average potential at a given applied current density, averaged over several experiments performed in this study. No experiment was performed using 1 M $CsHCO_3$ at 150 mA/cm^2.

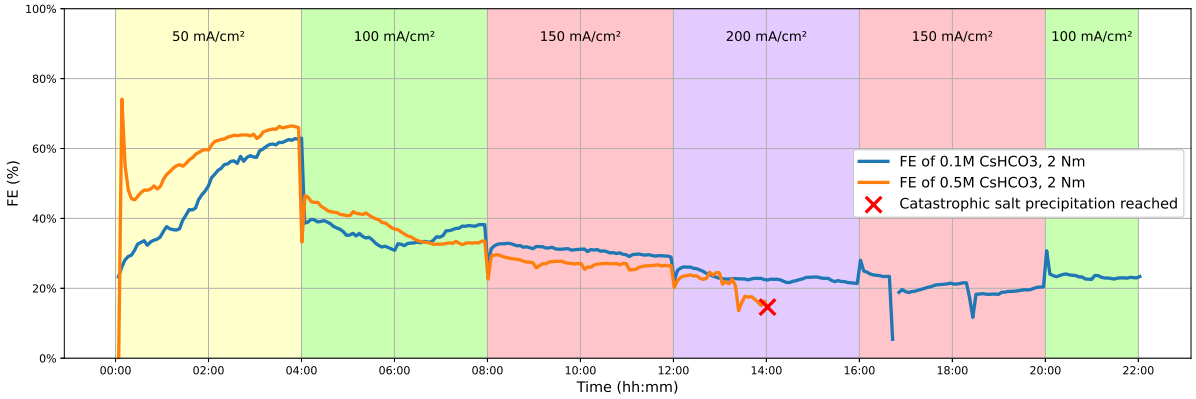

Figure 4.15: FE_{CO} over time of the 0.1M and 0.5M $CsHCO_3$ concentration experiment in 2 Nm-compressed CFE.

resenting the 0.5 M electrolyte experiment begins to lag in the 100 mA/cm^2 current-density phase (first green region) and ultimately reaches catastrophic salt blockage. Therefore, our observation suggests that in the long run, electrolyte concentration has a more substantial effect on salt precipitation than on promoting selectivity.

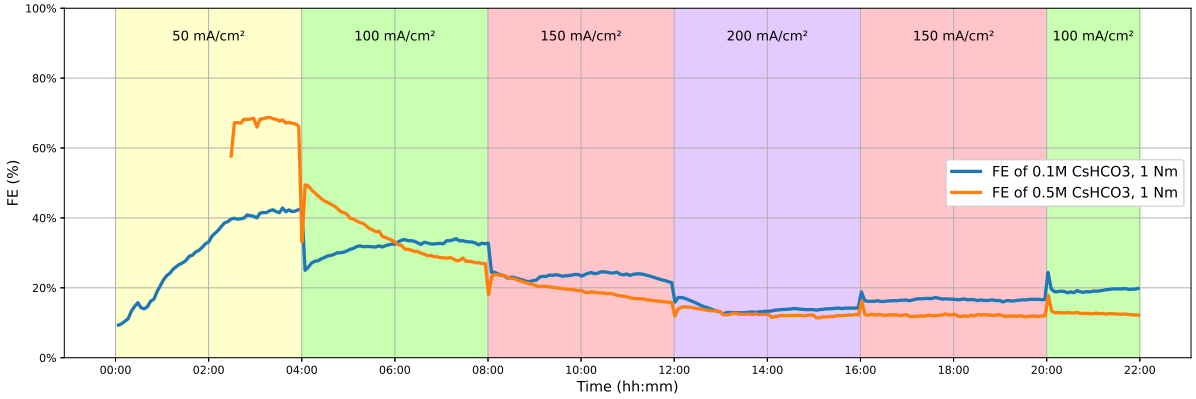

Figure 4.16: FE_{CO} over time of the 0.1M and 0.5M $CsHCO_3$ concentration experiment in 1 Nm-compressed CFE.

This trend is also observed in the comparison employing a 1 Nm-compressed cell shown in Figure 4.16. In this comparison, the experiment with 0.5 M electrolyte concentration again starts with higher FE_{CO}, but then gets progressively reduced performance until it performs slightly worse than the experiment with 0.1 M concentration. This worsening of performance

can also be attributed to the increase in salt buildup over time. The buildup of salt precipitates in the experiment with 0.5 M electrolyte is confirmed by the image in Figure 4.17 below, showing the visibly formed salt deposits. In this particular experiment, the salt deposits formed in the bottom rows of the flow channel rather than in the upper rows, as observed in every other experiment yielding visible salt deposits. We cannot yet explain this deviation. However, the salts deposited in the bottom rows explain how the experiment could still run without experiencing catastrophic salt precipitation, since the CO_2 feed gas entering through the top nozzles is no longer immediately blocked. Meanwhile, no salt deposit is visible in the flow channel of the experiment with 0.1 M electrolyte concentration.

Figure 4.17: Heavy salt precipitation in the bottom rows of the cathode flow channel in the experiment with 0.5 M $CsHCO_3$.

From these two comparisons, we can conclude that in the longer run, the advantage of higher electrolyte concentration on selectivity might be outweighed by its impact on salt formation. Given that a 0.1 M electrolyte concentration yields a lower FE_{CO} while the higher 0.5 M electrolyte concentration shows increased salt precipitation, we can conclude that there must be an optimum concentration value between that of 0.1 M and 0.5 M, where FE_{CO} and stability are maximized. A more rigorous sensitivity experiment is needed to find such an optimum.

Nevertheless, employing an electrolyte with 0.1 M concentration does not guarantee the absence of salt precipitates. We performed another instance of the experiment at a 0.1 M electrolyte concentration and 1 Nm of compression. This time, catastrophic salt precipitation occurs after 20 hours, just 2 hours before the experiment ends. We conclude that performing experiments with the exact same configuration and obtaining different salt precipitation behavior indicates that salt formation is an inherently stochastic process that can be affected by factors beyond standard laboratory control. Using a lower electrolyte concentration reduces the risk of catastrophic salt precipitation, but does not eliminate it deterministically.

4.4.3. CO_2 Feed Humidification

Lastly, we compare the effects of feeding CO_2 with different humidification levels: 0%, 80%, and 100%. As shown in Figure 4.18, both the 80% and the 100%-humidified CO_2 experiments get catastrophic salt precipitation after about 14 hours, indicated by the increase in upstream pressure to a maximum of 2.8 bars. Meanwhile, the upstream pressure in the experiment with dry or 0% humidified CO_2 only reached 0.1 bar after 15 hours, then rose to only 0.44 bar by the end of the experiment. This smaller increase could indicate a lesser extent of salt-precipitation blockage that does not completely obstruct gas flow.

Additionally, FE_{CO} is highest at 0% humidification and decreases progressively with higher humidification rates. These results suggest that in a CFE cell, reduced humidification of the CO_2 feed improves performance. This conclusion contrasts with what is commonly reported, in which some humidification is required to prevent the cell from drying out [69]. Hoof et al [67] suggest that 80% humidification provides optimal performance since full humidification will flood the GDE pores. Other reports also mention that providing humidification prevents salt precipitation [28, 70].

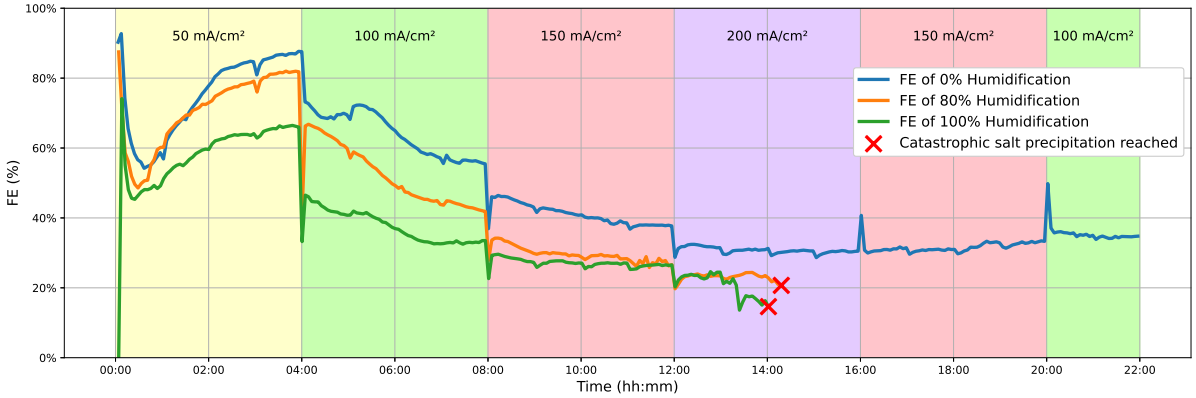

Figure 4.18: FE_{CO} over time of experiment with the feed CO_2 humidified to 0%, 80%, and 100% relative humidity.

This contrasting effect of feed CO_2 humidification in our CFE setup is probably because our GDE is already sufficiently humid from contact with the wet PES membrane, such that adding more water only worsens performance. The initial voltage peak, which includes a kinetic overpotential contribution, could also help erode the hydrophobicity of the cathode surface, a phenomenon that does not occur in a conventional cell. This additional reduction in hydrophobicity, unique to CFE cells, could exacerbate water imbibition and, subsequently, salt precipitation within the GDE.

4.5. Comparing CFE and Hybrid-MEA Cell Configuration

To benchmark the performance of our CFE cell, we compare it against a hybrid-MEA cell configuration. To ensure a fair comparison, the benchmark cell is constructed with identical components. The only differences are the use of AEM as a separator membrane and the anolyte flow of the hybrid-MEA setup.

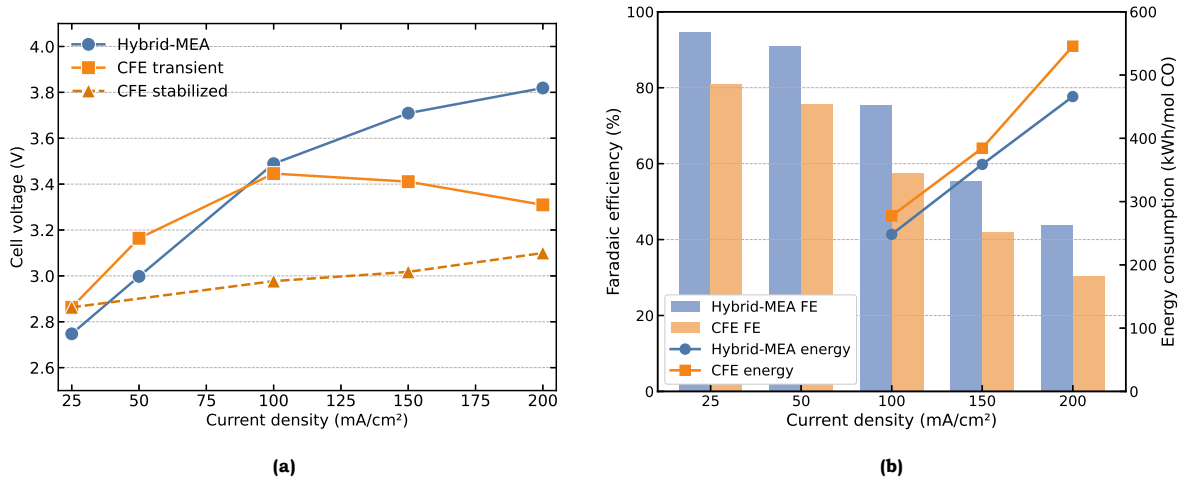

Figure 4.19: Comparison of Hybrid-MEA and CFE configuration: (a) voltages and (b) FE_{CO} and energy consumption at the last three current densities. The voltage plot shows the transient and the stabilized voltage measurement of the CFE cell.

Figure 4.19 shows the voltage, FE_{CO}, and energy consumption comparison of the two configurations. The voltage measurement of the CFE cell is shown with two lines: the transient voltage (solid orange line), which is the average voltage at which the Faradaic efficiency measurement is taken, and the stabilized voltage (dashed orange line), which is the voltage measured after the experiment had run for a few hours. The transient voltage is higher because, at the time of measurement, the tail of the initial voltage peak still dominates the measured

value. The effect can be observed by realizing that the transient voltage value at 200 mA/cm^2 is lower than at 150 mA/cm^2, which is also lower than at 100 mA/cm^2, indicating that the voltage still continuously decreases during measurement. Meanwhile, the stabilized voltage is the measured voltage after the initial voltage peak had completely subsided.

From the voltage comparison in Figure 4.19a, the CFE cell exhibits much lower voltage at higher current densities compared to the hybrid-MEA cell. The lower overall voltage could be a result of reduced anodic bubble formation from the absence of bulk liquid flow at the anode, in line with the reports from Hodges et al [11] and Hoang et al [12].

The comparison in Figure 4.19b shows lower FE_{CO} for CFE at all applied current densities. This lower faradaic efficiency of our CFE setup could be explained by extra cathode flooding due to proximity to the wet membrane, complemented by a possible added reduction in hydrophobicity induced by the initial increase in kinetic overpotential during the initial voltage peak. The figure also plots the calculated energy consumption for producing 1 mole of CO with either cell. The stabilized voltage is used to calculate the energy consumption of the CFE cell. With lower FE_{CO}, the energy consumed by the CFE cell to produce one mole of CO is above that of the hybrid-MEA cell despite the lower voltage. At 200 mA/cm^2, the CFE cell needs 545.65 kWh/mol CO while the hybrid-MEA consumes 465.98 kWh/mol CO. This result underscores the need for further research to improve the product selectivity of the CFE cell.

In its current state, the main issues with our CFE configuration are cathode flooding and salt formation, which hinder stable, long-term operation at high selectivity. Reduced hydrophobicity, whether due to reversible electrowetting or irreversible chemical degradation of PTFE, is commonly reported as the primary cause of flooding and subsequent salt precipitation. However, in CFE cells, we have hypothesized that high surface hydrophobicity might inhibit the detachment of degassed CO_2 bubbles from the cathode surface, thereby increasing the initial cell voltage. The resulting high voltage could, in turn, accelerate hydrophobicity loss. If this mechanism is correct, making the cathode surface more hydrophobic to resist water intrusion seems futile, since the induced high voltage would be expected to reduce hydrophobicity regardless. Further experimental work on the effect of surface hydrophobicity is required to verify whether this feedback mechanism governs the behavior of CFE cells. Another avenue of research could be porous membrane engineering to enable delivery of an optimal capillary flow rate, thereby avoiding both cathode flooding and salt supersaturation. A covering layer that can limit water spillage, placed on the membrane's cathode-facing side, could also be a potential solution. The proposed experimental pathway for the hydrophobicity effect and porous membrane is explained in Chapter 6 (Recommendations for future work).

Despite the need for further research to address these issues, the CFE for CO_2-to-CO conversion presented in this study has demonstrated several advantages over the conventional setup. First, the consistently lower voltage confirms the CFE cell's low-voltage operation. Further parametric optimization of the CFE cell, particularly on membrane pore size and cell compression, will be needed to improve product selectivity and lower per-mole product energy consumption. A survey study on techno-economic assessment of low-temperature CO_2 electrolysis found that electricity costs could account for up to 80% of OPEX [71]. Improved energy efficiency could then significantly lower the cost of producing a unit amount of CO and help close the gap toward commercial viability.

Cost reduction also comes from the simplified balance-of-plant, for example, by the lack of electrolyte circulating through the cell, which removes the need for a circulation pump. This component reduction contributes to the energy-efficiency gain and potentially reduces both CAPEX and OPEX of a CO_2RR electrolyzer plant. The use of cheaper porous membranes compared with the more expensive ion exchange membranes used in conventional cells further adds to the cost reduction.

This use of porous membranes, such as PES, is also a more environmentally friendly option due to the non-use of PFAS substances. PFAS (per- and polyfluoroalkyl substances), also

nicknamed ”forever chemicals”, are substances that contain very strong C-F bonds. This extreme stability makes them resistant to natural breakdown processes, which could then bioaccumulate in humans and wildlife [72]. Ion-exchange membranes such as Nafion use PTFE as a backbone, which is a PFAS [73]. While AEMs such as PiperIon are PFAS-free, their reinforced variants could contain PTFE [74]. The European Commission is currently proposing an EU-wide ban on all kinds of PFAS [75]. Once this restriction is in effect, and while a safer alternative is still under development, porous membrane utilizing cells can be a viable option.

5

Conclusion

This thesis project aims to implement the recent capillary-fed cell architecture idea for CO_2-to-CO conversion. The concept has been proven to work; however, an initial voltage peak unique to the CFE configuration for CO_2 electrolysis is identified, which has not been reported in any other work. We also found that water management strongly affects the stability of a CFE cell's performance. The use of a porous membrane enables additional controllability in this regard not found in other cell architectures.

Based on our investigation, the initial voltage peak is thought to be triggered by the formation of CO_2 bubbles inside the PES membrane pore matrix. The CO_2 bubbles are formed by neutralization of the crossing over (bi)carbonates by the acid environment inside the membrane near the anode. This claim is supported by the absence of an initial voltage peak when the (bi)carbonate source is removed or when the location of the neutralization reaction is moved from inside the membrane to outside it. To achieve this, we performed water electrolysis experiments in CsOH and $CsHCO_3$ electrolytes with the CFE setup. The experiment with CsOH exhibited no initial voltage peak, while the experiment with $CsHCO_3$ produced an initial voltage peak of much smaller magnitude, owing to the absent (bi)carbonate regeneration. In the other experiment, we placed an AEM between the anode and the PES membrane, which also shows no initial voltage peak. This placement prevents anode acidification from extending into the membrane, thereby moving (bi)carbonate neutralization to occur outside the membrane.

The presence of bubbles stuck in the membrane pores reduces the effective conductivity of the electrolyte, thus increasing the ohmic overpotential. The smaller the pore size, the harder it is for the bubbles to dislodge and therefore the higher the induced increase in ohmic overpotential. Furthermore, the cathode contributes to the increase in overpotential, as evidenced by a temporary shift in selectivity toward HER coinciding with the voltage peak. It is thought that the formed CO_2 bubbles accumulate on the cathode surface. This bubble accumulation can be caused by the absence of a gap through which the bubbles could escape or by high surface hydrophobicity that prevents bubbles from detaching from the surface. Regardless of the underlying mechanism, partial bubble coverage of the cathode surface increases the local current density of the uncovered active area. The increased local current density naturally increases the kinetic overpotential and causes an observable, temporary selectivity shift toward HER as the CO_2 reactant becomes mass-transport limited.

Next, design principles to enable more effective implementation are investigated. We found that, beyond the period when bubble dynamics dominate, water management is the key factor governing the stability of the CFE cell's performance. In our study, water management can be achieved by configuring the pore size of the capillary membrane, the tightness of the bolts that compress the cell, and the humidity level of the CO_2 feed gas. A larger pore size and lesser compression increase the amount of electrolyte liquid the membrane can deliver via capillary action. Therefore, the optimal flow rate can be tuned by configuring the membrane pore size

and the cell compression level. A higher flow rate increases the water surplus the cell receives, leading to increased cathode flooding and blocking gas transport. Conversely, too low a flow rate risks oversaturation of the electrolyte salt as water is consumed by the cathodic reaction, which accelerates salt precipitation. Additionally, higher electrolyte concentrations increase the probability of catastrophic salt precipitate formation, while too low a concentration may be insufficient to promote optimal product selectivity. Therefore, optimizing water supply and electrolyte concentration are key to stable CFE cell performance.

Compared with a conventional MEA cell architecture, the CFE cell exhibits lower overpotential at the higher current densities tested. This result confirms the low-voltage operation for the CFE configuration reported in previous works. However, the overall selectivity for the CO product remains lower, which could be explained by the higher rate of cathode flooding. The lower selectivity results in the CFE cell's energy consumption exceeding that of a hybrid-MEA cell. Thus, more research is still needed to improve product selectivity at higher current densities and performance stability, particularly regarding gas-transport-blocking cathode flooding and salt formation. Nevertheless, the simplified system setup and the use of cheaper membrane material in a CFE cell allow for a lower system cost, enhancing the economic feasibility of CO_2-to-CO conversion and synthetic fuel as a decarbonization pathway.

6

Recommendations for future work

Optimize the supply of water
Based on the identified water management design principles, a moderate capillary flow rate and a large membrane pore size are considered preferable for stable operation of a CFE cell. The moderate capillary flow rate is determined by the balance between cathode flooding and salt supersaturation. The large membrane pore size is used to reduce blockages by the CO_2 bubbles at the membrane pores. An experiment to try is to use a PES membrane with a larger pore size and offset it by tightening the compression, thereby yielding a net reduction in flow rate while preventing formed bubbles from becoming stuck in the pores.

Study on the effect of cathode surface hydrophobicity
In our study of the CFE cell for CO_2 electrolysis, an initial voltage peak is always observed. However, its effect on the long-term performance of the CFE cell needs further confirmation. We hypothesize that the increased voltage contains an increased kinetic overpotential component, which accelerates hydrophobicity degradation of the cathode surface in the first minutes of the experiment. To test the hypothesis, a set of experiments can be conducted by measuring the contact angle of the cathode surface before and after electrolysis with CFE and a conventional architecture. By knowing the baseline contact angle reduction in a conventional cell where the initial voltage peak is absent, the effect of having an initial voltage peak on cathode hydrophobicity can be determined.

Next, surface hydrophobicity is also suspected to contribute to the increased voltage by increasing bubble adhesion to the cathode surface. To test this hypothesis, a set of experiments can be performed with cathodes of different surface hydrophobicity and the resulting voltage peak height observed.

Finally, surface hydrophobicity must be high to prevent the cathode from flooding. If the previous experiments confirm that the initial voltage peak causes more hydrophobicity reduction and starting with a less hydrophobic surface reduces the initial voltage peak, then the CFE cell design problem faces a dilemma: starting with high surface hydrophobicity could result in aggressive degradation while starting with a low surface hydrophobicity results in low selectivity due to excessive flooding. Therefore, we hypothesize that there is an optimal starting surface hydrophobicity at which the corresponding initial voltage peak yields the highest hydrophobicity retention. To test this hypothesis, contact angles can be measured before and after experiments across a set of experiments with different starting surface hydrophobicity levels to identify the optimal choice.

Study on the multiphase dynamics inside the CFE cell
Following a different optimization approach, a multiphase numerical modeling study can be performed to show the species distribution across the membrane thickness. Special attention could be given to better understand the developing pH gradient and the (bi)carbonate neutralization to CO_2 gas bubble reaction inside the membrane. With the mechanism under-

stood, a better design of the membrane pore matrix or an optimized electrolyte concentration could be developed to improve bubble dispersion.

Imaging techniques that allow direct observation of the multiphase dynamics inside the zero-gap cell construction can also be employed. For example, X-rays have been employed to study bubble evolution in an electrolysis cell gap [76]. Such a technique can also be applied to our CFE cell to help clarify our understanding of bubble evolution, thought to govern the already discussed initial voltage peak. Moreover, neutron tomography has been used to uncover water distribution and salt precipitation in a zero-gap cell [43]. This method is relevant for clarifying the importance of water management in governing the stability of the CFE cell. By studying water coverage and availability across different regions within the cell under different operating conditions, more informed design considerations can be derived to enable effective CFE for CO_2-to-CO conversion.

Study on porous membranes
In our experiments, we found that our cathode is probably too wet, as evidenced by the significant effect of water management on FE_{CO} stability and by its lower value compared to an AEM hybrid-MEA cell. Therefore, finding ways to control the water supply would be an interesting avenue of research. One idea is to add a layer with lower water permeability than the porous membrane material, coated on the cathode-facing side of the porous membrane. The coating could prevent excessive wetting of the cathode, preventing it from being flooded.

The porous membrane also introduces the trapped CO_2 bubble problem, as already extensively discussed. Another potential fix for this issue is to use a highly hydrophilic material for the membrane to prevent bubbles from attaching to the pore walls. This approach has been demonstrated in water electrolysis by applying a hydrophilic hydrogel coating to promote bubble detachment, thereby minimizing ohmic and concentration overpotentials [77].

AI Use Statement

In this work, AI agents are used for different purposes. Literature searches are aided primarily by using Anara and Consensus. All material found by those agents is then manually checked against the original manuscript to ensure alignment. VS Code Copilot is used to aid with the generation of some of the Python scripts for plotting the data. In the writing process, Claude is used to generate LaTeX formatting scripts while Grammarly is used to help with spelling and grammar correction.

Acknowledgements

I would like to thank and commend Sten, my supervisor, for his patience and thorough support during the entirety of this project, especially when I was still clueless about pretty much everything. Thank you for the guidance and the fruitful discussions. Thank you also to David for letting me be a part of the EFS group and for the inputs and support throughout this project. I would also like to thank the PhDs, postdocs, technicians, and my other lab mates for the check-ups, occasional jokes, and the help here and there. Without you, my time spent on TNW 58 wouldn't be as fun.

To my housemates, Rifa, Rizqi, and (former housemate) Mas Hanif, thank you for the stories, foods, and all our time together. To the gang: Rizqi, Vadya, Ammar, Kak Grase, and Cetta, my bedrock of social life here, thank you for the invaluable bond. To Mas Aziis, with whom we share each other's struggles and also memes. To my SET 2024 friends, BP PPI Delft 24/25, and the rest of my Indonesian colleagues here. Also, to my dear Julia, who has accompanied me through it all. Without her, this thesis journey would have been a completely different experience, thank you.

And to Ibu and Ayah, thank you for your endless prayers. Can't wait to meet you home.

Thoriq Fauzan Ariandi
Delft, July 2026

Bibliography

[1] M. Jayachandran et al. “Challenges and Opportunities in Green Hydrogen Adoption for Decarbonizing Hard-to-Abate Industries: A Comprehensive Review”. In: *IEEE Access* 12 (2024), pp. 23363–23388. DOI: 10.1109/access.2024.3363869.

[2] Nathan Gray et al. “Decarbonising Ships, Planes and Trucks: An Analysis of Suitable Low-Carbon Fuels for the Maritime, Aviation and Haulage Sectors”. In: *Advances in Applied Energy* 1 (Feb. 2021), p. 100008. ISSN: 2666-7924. DOI: 10.1016/j.adapen.2021.100008.

[3] Blanca Belsa, Lu Xia, and F. Pelayo García de Arquer. “CO2 Electrolysis Technologies: Bridging the Gap toward Scale-up and Commercialization”. In: *ACS Energy Letters* 9.9 (Aug. 2024), pp. 4293–4305. ISSN: 2380-8195. DOI: 10.1021/acsenergylett.4c00955.

[4] Yoshio Hori, Katsuhei Kikuchi, and Shin Suzuki. “Production of CO and CH4 in electrochemical reduction of CO2 at metal electrodes in aqueous hydrogencarbonate solution”. In: *Chemistry letters* 14.11 (1985), pp. 1695–1698.

[5] Drew Higgins et al. “Gas-Diffusion Electrodes for Carbon Dioxide Reduction: A New Paradigm”. In: *ACS Energy Letters* 4.1 (Jan. 2019), pp. 317–324. DOI: 10.1021/acsenergylett.8b02035.

[6] Xuerong Wang et al. “Designing Membrane Electrode Assembly for Electrochemical CO2 Reduction: A Review”. In: *Transactions of Tianjin University* 30.2 (Apr. 2024), pp. 117–129. ISSN: 1995-8196. DOI: 10.1007/s12209-024-00390-5.

[7] Rainer Küngas. “Review—Electrochemical CO2 Reduction for CO Production: Comparison of Low- and High-Temperature Electrolysis Technologies”. In: *Journal of The Electrochemical Society* 167.4 (Feb. 2020), p. 044508. ISSN: 1945-7111. DOI: 10.1149/1945-7111/ab7099.

[8] Lorenz M. Baumgartner et al. “Electrowetting Limits Electrochemical CO 2 Reduction in Carbon-Free Gas Diffusion Electrodes”. In: *Energy Advances* 2.11 (2023), pp. 1893–1904. DOI: 10.1039/D3YA00285C.

[9] Joshua A. Rabinowitz and Matthew W. Kanan. “The Future of Low-Temperature Carbon Dioxide Electrolysis Depends on Solving One Basic Problem”. In: *Nature Communications* 11.1 (Oct. 2020), p. 5231. ISSN: 2041-1723. DOI: 10.1038/s41467-020-19135-8.

[10] Mahinder Ramdin et al. “Electroreduction of CO_2 /CO to C_2 Products: Process Modeling, Downstream Separation, System Integration, and Economic Analysis”. In: *Industrial & Engineering Chemistry Research* 60.49 (Dec. 2021), pp. 17862–17880. ISSN: 0888-5885, 1520-5045. DOI: 10.1021/acs.iecr.1c03592.

[11] Aaron Hodges et al. “A High-Performance Capillary-Fed Electrolysis Cell Promises More Cost-Competitive Renewable Hydrogen”. In: *Nature Communications* 13.1 (Mar. 2022), p. 1304. ISSN: 2041-1723. DOI: 10.1038/s41467-022-28953-x.

[12] Anh Linh Hoang et al. “Bubble Detection on the Cathode and Anode of a High-Performing Capillary-Fed Water Electrolysis Cell”. In: *Sustainable Energy & Fuels* 7.18 (2023), pp. 4450–4460. ISSN: 2398-4902. DOI: 10.1039/D3SE00744H.

[13] Shubhi Tripathi et al. “Studies on Capillary-Induced Electrolyte Flow Phenomenon for Hydrogen Production in Acidic Media”. In: *ChemCatChem* (Sept. 2025), e01074. ISSN: 1867-3880, 1867-3899. DOI: 10.1002/cctc.202501074.

[14] Woong Hee Lee et al. “New Strategies for Economically Feasible CO2 Electroreduction Using a Porous Membrane in Zero-Gap Configuration”. In: *Journal of Materials Chemistry A* 9.29 (July 2021), pp. 16169–16177. ISSN: 2050-7496. DOI: 10.1039/D1TA03182A.

[15] Shilei Wei et al. “Porous Membranes Enable Selective and Stable Zero-Gap Acidic CO2 Electrolysers”. In: *Nature Communications* 16.1 (Oct. 2025), p. 9299. ISSN: 2041-1723. DOI: 10.1038/s41467-025-64342-w.

[16] Min Gwan Ha et al. “Efficient and Durable Porous Membrane-Based CO2 Electrolysis for Commercial Zero-Gap Electrolyzer Stack Systems”. In: *Chemical Engineering Journal* 496 (Sept. 2024), p. 154060. ISSN: 13858947. DOI: 10.1016/j.cej.2024.154060.

[17] Xiaolong Zhang et al. “Electrocatalytic Carbon Dioxide Reduction: From Fundamental Principles to Catalyst Design”. In: *Materials Today Advances* 7 (Sept. 2020), p. 100074. ISSN: 2590-0498. DOI: 10.1016/j.mtadv.2020.100074.

[18] Yao Yao, Ernest Pahuyo Delmo, and Minhua Shao. “The Electrode/Electrolyte Interface Study during the Electrochemical CO2 Reduction in Acidic Electrolytes”. In: *Angewandte Chemie* 137.4 (2025), e202415894. ISSN: 1521-3757. DOI: 10.1002/ange.202415894.

[19] Weixing Wu and Ying Wang. “The Role of Protons in CO2 Reduction on Gold under Acidic Conditions”. In: *Journal of the American Chemical Society* 147.14 (Apr. 2025), pp. 11662–11666. ISSN: 0002-7863. DOI: 10.1021/jacs.5c01149.

[20] Binbin Pan et al. “Close to 90% Single-Pass Conversion Efficiency for CO2 Electroreduction in an Acid-Fed Membrane Electrode Assembly”. In: *ACS Energy Letters* 7.12 (Dec. 2022), pp. 4224–4231. DOI: 10.1021/acsenergylett.2c02292.

[21] Mariana C. O. Monteiro et al. “The Role of Cation Acidity on the Competition between Hydrogen Evolution and CO2 Reduction on Gold Electrodes”. In: *Journal of the American Chemical Society* 144.4 (Feb. 2022), pp. 1589–1602. ISSN: 0002-7863. DOI: 10.1021/jacs.1c10171.

[22] Meenesh R. Singh et al. “Hydrolysis of Electrolyte Cations Enhances the Electrochemical Reduction of CO2 over Ag and Cu”. In: *Journal of the American Chemical Society* 138.39 (Sept. 2016). ISSN: 0002-7863. DOI: 10.1021/jacs.6b07612.

[23] Saket S. Bhargava et al. “System Design Rules for Intensifying the Electrochemical Reduction of CO2 to CO on Ag Nanoparticles”. In: *ChemElectroChem* 7.9 (2020), pp. 2001–2011. ISSN: 2196-0216. DOI: 10.1002/celc.202000089.

[24] Mariana C. O. Monteiro et al. “Absence of CO2 Electroreduction on Copper, Gold and Silver Electrodes without Metal Cations in Solution”. In: *Nature Catalysis* 4.8 (Aug. 2021), pp. 654–662. ISSN: 2520-1158. DOI: 10.1038/s41929-021-00655-5.

[25] Binbin Pan, Yuhang Wang, and Yanguang Li. “Understanding and Leveraging the Effect of Cations in the Electrical Double Layer for Electrochemical CO2 Reduction”. In: *Chem Catalysis* 2.6 (June 2022), pp. 1267–1276. ISSN: 2667-1093. DOI: 10.1016/j.checat.2022.03.012.

[26] Shintaro Kato et al. “Quantitative Analysis and Manipulation of Alkali Metal Cations at the Cathode Surface in Membrane Electrode Assembly Electrolyzers for CO2 Reduction Reactions”. In: *ChemSusChem* 17.22 (2024), e202401013. ISSN: 1864-564X. DOI: 10.1002/cssc.202401013.

[27] Lien-Chun Weng, Alexis T. Bell, and Adam Z. Weber. “Towards Membrane-Electrode Assembly Systems for CO_2 Reduction: A Modeling Study”. In: *Energy & Environmental Science* 12.6 (2019), pp. 1950–1968. ISSN: 1754-5692, 1754-5706. DOI: 10.1039/C9EE00909D.

[28] Jasper Biemolt et al. “Preventing Salt Formation in Zero-Gap CO_2 Electrolyzers by Quantifying Cation Accumulation”. In: *ACS Energy Letters* 10.2 (Feb. 2025), pp. 807–814. ISSN: 2380-8195, 2380-8195. DOI: 10.1021/acsenergylett.4c03242.

[29] Sahil Garg et al. “How Alkali Cations Affect Salt Precipitation and CO_2 Electrolysis Performance in Membrane Electrode Assembly Electrolyzers”. In: *Energy & Environmental Science* 16.4 (2023), pp. 1631–1643. ISSN: 1754-5692, 1754-5706. DOI: 10.1039/D2EE03725D.

[30] Nathan T. Nesbitt et al. “Liquid–Solid Boundaries Dominate Activity of CO2 Reduction on Gas-Diffusion Electrodes”. In: *ACS Catalysis* 10.23 (Dec. 2020), pp. 14093–14106. DOI: 10.1021/acscatal.0c03319.

[31] Julie C. Fornaciari et al. “Mechanistic Understanding of pH Effects on the Oxygen Evolution Reaction”. In: *Electrochimica Acta* 405.LLNL-JRNL-837583; NREL/JA–5900-81947 (Dec. 2021). ISSN: 0013-4686. DOI: 10.1016/j.electacta.2021.139810.

[32] Samuel S. Veroneau et al. “A Straightforward Model for Quantifying Local pH Gradients Governing the Oxygen Evolution Reaction”. In: *Journal of the American Chemical Society* 146.42 (Oct. 2024). ISSN: 1520-5126. DOI: 10.1021/jacs.4c09521.

[33] Takeshi Nishimoto et al. “Delivering the Full Potential of Oxygen Evolving Electrocatalyst by Conditioning Electrolytes at Near-Neutral pH”. In: *ChemSusChem* 14.6 (Mar. 2021), pp. 1554–1564. ISSN: 1864-5631, 1864-564X. DOI: 10.1002/cssc.202002813.

[34] Thomas F Fuller and John N Harb. *Electrochemical engineering*. John Wiley & Sons, 2018.

[35] Alexis T. Bell. “Understanding the Effects of Composition and Structure on the Oxygen Evolution Reaction (OER) Occurring on NiFeOx Catalysts”. In: (Sept. 2018). DOI: 10.1039/9781788010313-00079. (Visited on 06/14/2026).

[36] Allen J Bard, Larry R Faulkner, and Henry S White. *Electrochemical methods: fundamentals and applications*. John Wiley & Sons, 2022.

[37] Christopher McCallum et al. “Reducing the Crossover of Carbonate and Liquid Products during Carbon Dioxide Electroreduction”. In: *Cell Reports Physical Science* 2.8 (Aug. 2021). ISSN: 2666-3864. DOI: 10.1016/j.xcrp.2021.100522.

[38] Xu Lu et al. “In Situ Observation of the pH Gradient near the Gas Diffusion Electrode of CO2 Reduction in Alkaline Electrolyte”. In: *Journal of the American Chemical Society* 142.36 (Sept. 2020), pp. 15438–15444. ISSN: 0002-7863. DOI: 10.1021/jacs.0c06779.

[39] R Mealy and G Bowman. “Importance of general chemistry relationships in water treatment”. In: *Handout Lab Hyg 1e47* (2019).

[40] Lorenz M. Baumgartner et al. “Narrow Pressure Stability Window of Gas Diffusion Electrodes Limits the Scale-Up of CO2 Electrolyzers”. In: *ACS Sustainable Chemistry & Engineering* 10.14 (Apr. 2022), pp. 4683–4693. DOI: 10.1021/acssuschemeng.2c00195.

[41] Fabian Bienen et al. “Investigating the Electrowetting of Silver-Based Gas-Diffusion Electrodes during Oxygen Reduction Reaction with Electrochemical and Optical Methods”. In: *Electrochemical Science Advances* 3.1 (2023), e2100158. ISSN: 2698-5977. DOI: 10.1002/elsa.202100158.

[42] Joost W. van Honschoten, Nataliya Brunets, and Niels R. Tas. “Capillarity at the Nanoscale”. In: *Chemical Society Reviews* 39.3 (Feb. 2010), pp. 1096–1114. ISSN: 1460-4744. DOI: 10.1039/B909101G.

[43] Joey Disch et al. “High-Resolution Neutron Imaging of Salt Precipitation and Water Transport in Zero-Gap CO2 Electrolysis”. In: *Nature Communications* 13.1 (Oct. 2022), p. 6099. ISSN: 2041-1723. DOI: 10.1038/s41467-022-33694-y.

[44] McLain E. Leonard et al. “Investigating Electrode Flooding in a Flowing Electrolyte, Gas-Fed Carbon Dioxide Electrolyzer”. In: *ChemSusChem* 13.2 (2020), pp. 400–411. ISSN: 1864-564X. DOI: 10.1002/cssc.201902547.

[45] Shaoyun Hao et al. “Improving the Operational Stability of Electrochemical CO2 Reduction Reaction via Salt Precipitation Understanding and Management”. In: *Nature Energy* 10.2 (Feb. 2025), pp. 266–277. ISSN: 2058-7546. DOI: 10.1038/s41560-024-01695-4.

[46] Bjørt Óladóttir Joensen et al. “Unveiling Transport Mechanisms of Cesium and Water in Operando Zero-Gap CO2 Electrolyzers”. In: *Joule* 8.6 (June 2024), pp. 1754–1771. ISSN: 2542-4785, 2542-4351. DOI: 10.1016/j.joule.2024.02.027.

[47] S. B. Iversen et al. “Characterization of Microporous Membranes for Use in Membrane Contactors”. In: *Journal of Membrane Science* 130.1 (July 1997), pp. 205–217. ISSN: 0376-7388. DOI: 10.1016/S0376-7388(97)00026-4.

[48] Dongdong Zhang et al. “Optimal Electrocatalyst Design Strategies for Acidic Oxygen Evolution”. In: *Advanced Science* 11.38 (2024), p. 2401975. ISSN: 2198-3844. DOI: 10.1002/advs.202401975.

[49] Ádám Vass et al. “Local Chemical Environment Governs Anode Processes in CO2 Electrolyzers”. In: *ACS Energy Letters* 6.11 (Nov. 2021), pp. 3801–3808. DOI: 10.1021/acsenergylett.1c01937.

[50] Sterlitech Corporation. *PES Membrane Filters Data Sheet*. Sterlitech Corporation. 2025. URL: https://www.sterlitech.com/media/amasty/amfile/attach/PES%20Membrane%20Filters%20Data%20Sheet.pdf.

[51] Jan-Willem Hurkmans et al. “Heating Dictates the Scalability of CO_2 Electrolyzer Types”. In: *EES Catalysis* 3.2 (2025), pp. 305–317. ISSN: 2753-801X. DOI: 10.1039/D4EY00190G.

[52] David L. Parkhurst and C. A. J. Appelo. *PHREEQC (Version 3) – A Computer Program for Speciation, Batch-Reaction, One-Dimensional Transport, and Inverse Geochemical Calculations*. Version 3. Thermodynamic database: `phreeqc.dat`. U.S. Geological Survey, 2013. URL: https://www.usgs.gov/software/phreeqc-version-3.

[53] Andrea Angulo et al. “Influence of Bubbles on the Energy Conversion Efficiency of Electrochemical Reactors”. In: *Joule* 4.3 (Mar. 2020), pp. 555–579. ISSN: 25424351. DOI: 10.1016/j.joule.2020.01.005.

[54] Rodrigo Lira Garcia Barros et al. “Impact of Nickel Electrode Geometry on the Electrochemical Performance and Bubble Dynamics of a Zero-Gap Alkaline Electrolyzer”. In: *Journal of Power Sources* 630 (Feb. 2025), p. 236116. ISSN: 0378-7753. DOI: 10.1016/j.jpowsour.2024.236116.

[55] Rui Wu et al. “Bubbles in Porous Electrodes for Alkaline Water Electrolysis”. In: *Langmuir* 40.1 (Jan. 2024), pp. 721–733. ISSN: 0743-7463, 1520-5827. DOI: 10.1021/acs.langmuir.3c02925.

[56] J. W. Haverkort and H. Rajaei. “Voltage Losses in Zero-Gap Alkaline Water Electrolysis”. In: *Journal of Power Sources* 497 (June 2021), p. 229864. ISSN: 0378-7753. DOI: 10.1016/j.jpowsour.2021.229864.

[57] W. L. van der Does, N. Valle, and J. W. Haverkort. “Bubble Resistance in Near-Zero-Gap Alkaline Water Electrolysis”. In: *Electrochimica Acta* 562 (June 2026), p. 148509. ISSN: 0013-4686. DOI: 10.1016/j.electacta.2026.148509.

[58] G. S. Shapoval et al. “Electrochemical Reductive Destruction of Polytetrafluoroethylene”. In: *Theoretical and Experimental Chemistry* 20.2 (1984), pp. 234–236. ISSN: 0040-5760, 1573-935X. DOI: 10.1007/BF00592820.

[59] Run Shi et al. “Efficient Wettability-Controlled Electroreduction of CO2 to CO at Au/C Interfaces”. In: *Nature Communications* 11.1 (June 2020), p. 3028. ISSN: 2041-1723. DOI: 10.1038/s41467-020-16847-9.

[60] Carlos Uriarte, Marco A. Fontelos, and Manuel Arrayás. *Phase Field Modelling of the Growth and Detachment of Bubbles in a Hydrogen Electrolyzer*. Dec. 2025. DOI: 10.48550/arXiv.2508.16585. eprint: 2508.16585 (cond-mat.soft).

[61] Daniel Wesley. “The Role of Surface Wettability on Bubble Formation in Air-Water Systems.” PhD thesis. University of Sheffield, Aug. 2015.

[62] Lijuan Sun et al. “Bubble Adhesion Dynamics on Solid Surfaces: Interfacial Behavior, Force, and Energy Perspectives Using a Self-Developed Dynamic Force Testing System”. In: *Separation and Purification Technology* 355 (Mar. 2025), p. 129651. ISSN: 1383-5866. DOI: 10.1016/j.seppur.2024.129651.

[63] Mateusz Kruszelnicki, Przemyslaw B. Kowalczuk, and Izabela Polowczyk. “Three-Phase Contact Formation between an Air Bubble and Solid Surfaces with Different Hydrophobicity Degrees in Liquid”. In: *Colloids and Surfaces A: Physicochemical and Engineering Aspects* 676 (Nov. 2023), p. 132067. ISSN: 0927-7757. DOI: 10.1016/j.colsurfa.2023.132067.

[64] John Dukovic and Charles W. Tobias. “The Influence of Attached Bubbles on Potential Drop and Current Distribution at Gas-Evolving Electrodes”. In: *Journal of The Electrochemical Society* 134.2 (Feb. 1987), p. 331. ISSN: 1945-7111. DOI: 10.1149/1.2100456.

[65] Huicui Chen et al. “Correlation Between Bubble Coverage and Current Density Distribution in a Proton Exchange Membrane Water Electrolyzer”. In: *Energies* 19.7 (Jan. 2026), p. 1754. ISSN: 1996-1073. DOI: 10.3390/en19071754.

[66] F. J. Higuera. “A Model of the Growth of Hydrogen Bubbles in the Electrolysis of Water”. In: *Journal of Fluid Mechanics* 927 (Nov. 2021), A33. ISSN: 0022-1120, 1469-7645. DOI: 10.1017/jfm.2021.778.

[67] Lucas Hoof et al. “Hidden Parameters for Electrochemical Carbon Dioxide Reduction in Zero-Gap Electrolyzers”. In: *Cell Reports Physical Science* 3.4 (Apr. 2022), p. 100825. ISSN: 26663864. DOI: 10.1016/j.xcrp.2022.100825.

[68] Péter Gyenes et al. “Flooding Revisited: Electrolyte Management Ensures Robust Electrochemical CO_2 Reduction”. In: *Energy & Environmental Science* 18.14 (2025), pp. 7124–7135. ISSN: 1754-5692, 1754-5706. DOI: 10.1039/D5EE01464F.

[69] Joey Disch et al. “Strategies for the Mitigation of Salt Precipitation in Zero-Gap CO 2 Electrolyzers Producing CO”. In: *Journal of Materials Chemistry A* 11.14 (2023), pp. 7344–7357. DOI: 10.1039/D2TA09966G.

[70] Danika G. Wheeler et al. “Quantification of Water Transport in a CO_2 Electrolyzer”. In: *Energy & Environmental Science* 13.12 (2020), pp. 5126–5134. ISSN: 1754-5692, 1754-5706. DOI: 10.1039/D0EE02219E.

[71] Josephine Vos, Andrea Ramírez, and Mar Pérez-Fortes. “Learning from the Past: Limitations of Techno-Economic Assessments for Low-Temperature CO2 Electrolysis”. In: *Renewable and Sustainable Energy Reviews* 213 (May 2025), p. 115454. ISSN: 13640321. DOI: 10.1016/j.rser.2025.115454.

[72] Xin Liu et al. “Photocatalytic C–F Bond Activation in Small Molecules and Polyfluoroalkyl Substances”. In: *Nature* 637.8046 (Jan. 2025), pp. 601–607. ISSN: 1476-4687. DOI: 10.1038/s41586-024-08327-7.

[73] Matteo Di Virgilio et al. “Functional and Environmental Performances of Novel Electrolytic Membranes for PEM Fuel Cells: A Lab-Scale Case Study”. In: *Clean Technologies* 5.1 (Mar. 2023), pp. 74–93. ISSN: 2571-8797. DOI: 10.3390/cleantechnol5010005.

[74] Fuel Cell Store. *PDT-20X Pt-Impregnated ePTFE Reinforced Anion Exchange Membrane*. https://www.fuelcellstore.com/pdt-20-pt-impregnated-eptfe-reinforced-aem-78010053. SKU: 78010053. Accessed: 2026-07-11. Fuel Cell Store.

[75] European Commission, Directorate-General for Environment. *PFAS Pollution*. https://environment.ec.europa.eu/topics/chemicals/pfas-pollution_en. Accessed: 2026-07-14. 2026.

[76] On-Yu Dung et al. “X-Ray Measurements of Gas Distribution in a Zero Gap Alkaline Water Electrolyzer”. In: *International Journal of Hydrogen Energy* 105 (Mar. 2025), pp. 835–844. ISSN: 0360-3199. DOI: 10.1016/j.ijhydene.2025.01.110.

[77] Misol Bae et al. “Superaerophobic Polyethyleneimine Hydrogels for Improving Electrochemical Hydrogen Production by Promoting Bubble Detachment”. In: *Advanced Energy Materials* 12.29 (2022), p. 2201452. ISSN: 1614-6840. DOI: 10.1002/aenm.202201452.

[78] Luca Bohn et al. “Reference Electrode Types for Zero-Gap CO_2 Electrolyzers: Benefits and Limitations”. In: *Advanced Science* 11.32 (Aug. 2024), p. 2402095. ISSN: 2198-3844, 2198-3844. DOI: 10.1002/advs.202402095.

A

Supporting Informations

A.1. Experiment Setup

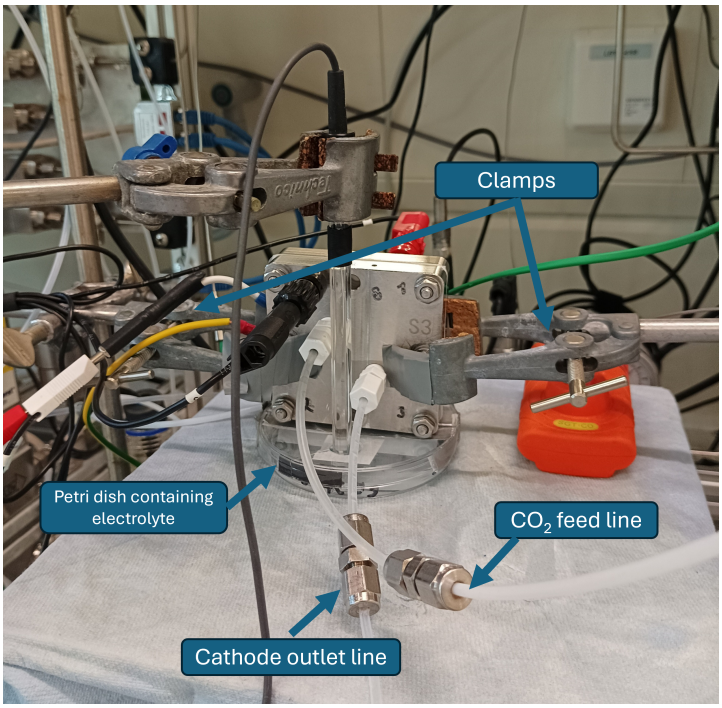

Figure A.1: Picture of the assembled and connected CFE cell.

Figure A.1 shows a picture of the CFE cell already assembled and connected to the gas lines. Two clamps are used to sustain the cell above the petri dish. The petri lid is placed to reduce the air-electrolyte surface contact area and limit evaporation during the longer-term experiments. A slit is cut on the lid to allow entry of the protruding PES membrane at the bottom of the cell.

An Ag/AgCl reference electrode is also dipped into the electrolyte and connected to the potentiostat, providing separate cathode and anode voltages. However, slight misalignment of the electrodes would compromise the voltage reading [78]. Since we cannot guarantee electrode alignment within the cell, the separate anodic and cathodic voltages are not included in the analysis.

A.2. Initial Voltage Peak Height Distribution

Figure A.2a shows the maximum peak heights of experiments with different PES membrane pore sizes while all other important parameters are identical. The experiment with a PES pore size of 1.2 μm was only performed once. The measured 8 V maximum peak height is inaccurate since it is the threshold voltage set as a safety feature for the potentiostat at that time of the experiment. If the threshold voltage setting was inactivated, the actual maximum peak height could reach higher values. Given that the 8 V peak height of the 1.2 μm pore size experiment is already much higher than the peak voltage range of the experiments with 5 μm, we can assume that the relationship would hold if more experimental samples were conducted. However, the voltage peak heights of the 8 μm membrane pore size experiments do not seem to be significantly different from the experiments with 5 μm membrane pore size. However, more data samples are required before a conclusion can be made.

Figure A.2b shows the maximum peak heights of experiments with different bolt compressions while keeping the other important parameters identical. Based on the results, bolt compression does not seem to affect the maximum height of the initial voltage peak. However, more data samples are also required for any conclusion to be made.

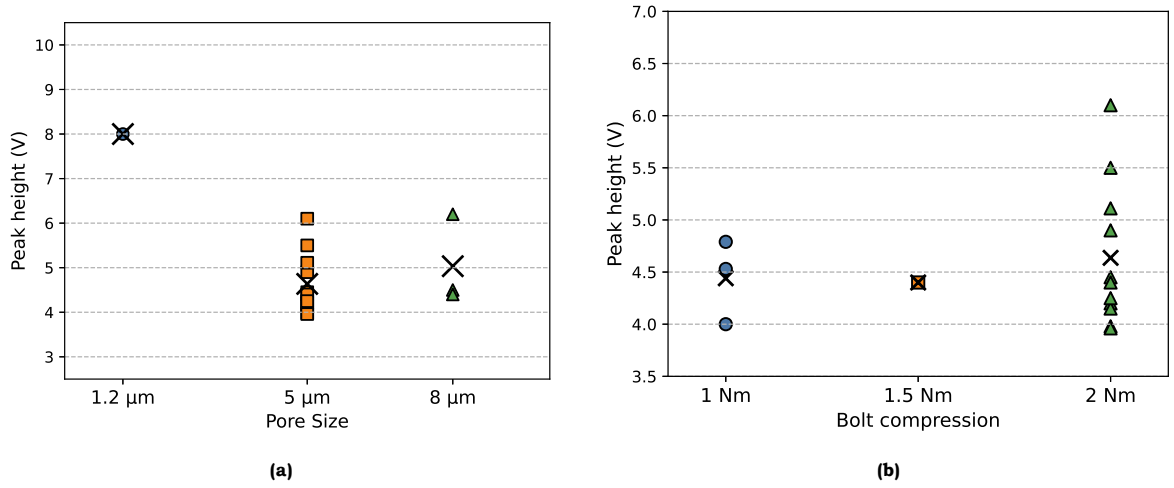

Figure A.2: Maximum initial voltage peak heights in experiments with 0.5 M $CsHCO_3$ and 50 mA/cm^2 current density in (a) PES membrane pore sizes 1.2 μm, 5 μm, and 8 μm performed with 2 Nm compression (b) Bolt compression of 1 Nm, 1.5 Nm, and 2 Nm performed with 5 μm PES pore size. The "X" marks the average maximum height.

A.3. Capillary Flow Rate Model

We model the estimated capillary flow rate at different heights of the PES membrane based on Equation 2.21 below:

$$Q = \frac{\varepsilon^2 A r \gamma_{LG} \cos\theta}{4(2-\varepsilon)^2 \mu L}$$

where ε is the porosity of the porous membrane, A is the cross sectional area of the membrane, r is the pore radius, γ_{LG} is the surface tension, θ is the contact angle representing the hydrophobicity of the membrane, μ is the viscosity of the electrolyte solution, and L is the column height.

To calculate the capillary flow rate, we define the variables as follows. The cross-sectional area of the membrane is its thickness multiplied by the width. Considering only the active area, the width is 2.25 cm. The membrane thickness decreases with higher bolt compression. For 2 Nm bolt compression, the membrane thickness is approximately 100 μm, while for 1 Nm bolt compression the thickness becomes approximately 120 μm. Thickness also affects the porosity of the membrane. Given that the uncompressed PES membrane is approximately

130 μm with 80% porosity [11], the compressed membrane porosity becomes 78.33% and 74% for 1 Nm and 2 Nm bolt compression, respectively. The contact angle of the PES membrane is reported to be 70.3^o. Meanwhile, surface tension, viscosity, and density are assumed using data for pure water as follows.

Surface tension (γ_{GL})	: 72.8 mN/m
Viscosity (μ)	: 1.002 mPa·s
Water density (ρ)	: 1 g/mL

Figure A.3 shows the plot of the modeled capillary flow rate along the height of the PES membrane for three scenarios: 1 Nm bolt compression in a 5 μm pore, 2 Nm bolt compression in a 1.2 μm pore, and 2 Nm bolt compression in a 5 μm. The purpose of this plot is to show the relative supply of water each scenario provides as opposed to providing accurate capillary flow rate prediction. The actual capillary flow rate will be affected by the electrolyte concentration and temperature, which affect the physical property values currently associated with pure water and the actual distribution of pore sizes within the membrane. Consumption of water in a certain height also affects the amount of water that can be supplied to the regions above it, further complicating accurate flow rate prediction.

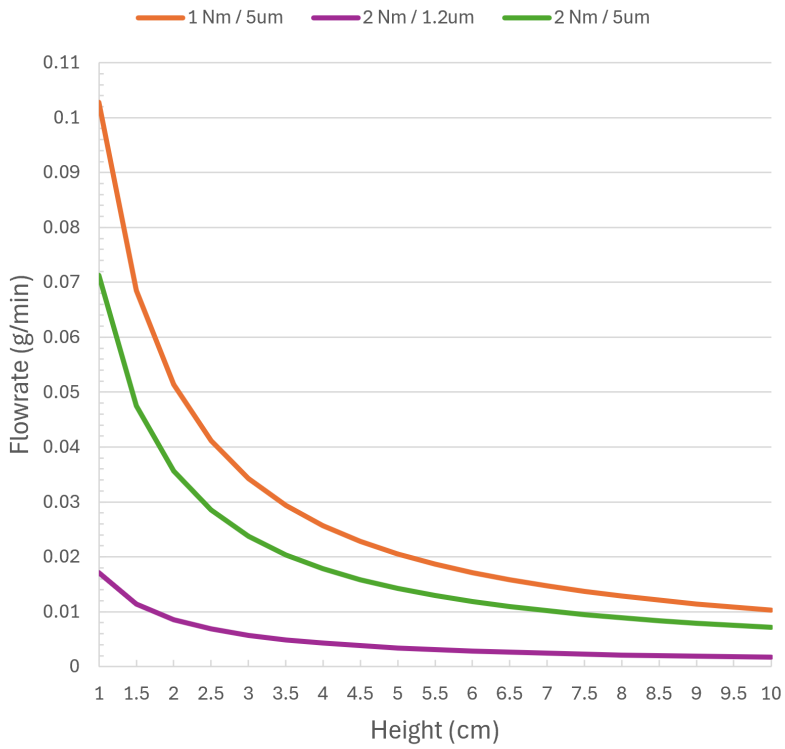

Figure A.3: Modeled capillary flow rates for different scenarios.

A.4. Experiment with Bottom-Fed CO_2 Gas

The comparison of the effect of bolt compression is repeated with the inlet CO_2 gas fed from the bottom nozzle, circumventing the salt deposits blocking the top entrance of the flow channel.

Figure A.4 shows the FE_{CO} evolution of the two experiments. In the first chronopotentiometry steps (50 mA/cm^2), the 1 Nm compressed cell exhibits higher FE_{CO}. In the next current step, the 1 Nm experiment saw a FE_{CO} drop, which continues to decrease until the FE_{CO} is lower than that of the 2 Nm experiment until the end of the experiment. This comparison confirms previous observations of more compressed CFE cells yielding higher FE_{CO}.

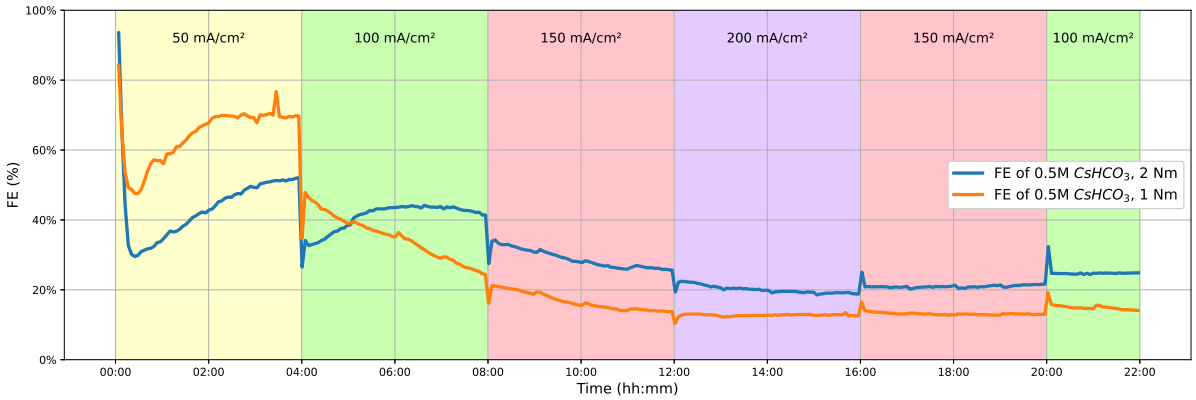

Figure A.4: FE_{CO} over time of the 2 Nm and 1 Nm-compressed CFE cell in 0.5 M $CsHCO_3$ with bottom-fed CO_2 feed gas.

Figure A.5 shows the salt formation at the cathode flow channel of the experiment with 2 Nm compression. The black layer at the top is a part of the cathode that sticks to the backplate during disassembly. From the image below, the bottom rows are free of salt deposits blocking, allowing the CO_2 gas to enter the cell and keep the cell running.

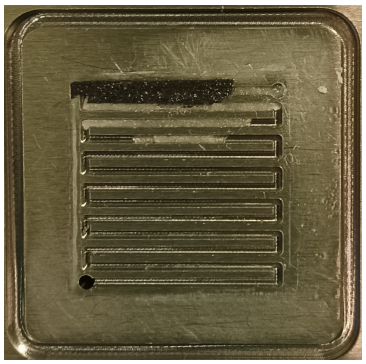

Figure A.5: Heavy salt precipitation in the upper rows of the cathode flow channel in the experiment with 2 Nm bolt compression with the CO_2 gas fed from the bottom nozzle.